Study on Atomistic Friction

（和訳：摩擦の原子論に関する研究）

１９９８年６月

平　野　元　久

Acknowledgments

I would like to acknowledge the kind and generous assistance that has been offered throughout the course of the work presented here.

I am grateful to Professor Shuji Hasegawa, Professor Hidetoshi Fukuyama, Professor Fumio Komori, Professor Atsushi Fujimori, and Professor Kimitoshi Kohno of The University of Tokyo for their guidance of this work.

I wish to express my deep gratitude to Dr. Kazumasa Shinjo of Advanced Telecommunications Research Institute International for his collaboration and for helpful discussions throughout this work.

I have also benefited from inspiring discussions with Professor Yoshitada Murata of The University of Electro-Communications, Professor Tatsuo Okano and Professor Katsuyuki Fukutani of The University of Tokyo, Professor Reizo Kaneko of Wakayama University (former Fellow of Kaneko Laboratory of NTT Interdisciplinary Research Laboratories), Professor Shigehisa Fukui of Tottori University (former Supervisor of Precise Control Research Group of NTT Interdisciplinary Research Laboratories), Professor Masafumi Senoo, Vice President of Mie University, Professor Nobuo Ohmae and Professor Hiroshi Matsukawa of Osaka University, Professor Akihito Matsumuro of Nagoya University, Professor Masamichi Fujihira and Dr. Takashi Nakano of Tokyo Institute of Technology, Professor Ken'ichi Hiratsuka of Chiba Institute of Technology, Professor Kohji Miura of Aichi University of Education, Dr. Tomonori Itoh of NTT Systems Electronics Laboratories, Professor Jean-Michel Martin of Ecole Centrale de Lyon, France, Professor Karsten Wedel Jacobsen of Technical University of Denmark, Denmark, and Dr. Irwin Singer of Naval Research Laboratories, USA for their technical advice and discussions.

This work was done at NTT Interdisciplinary Research Laboratories (NTT-IRL) and NTT Integrated Information & Energy Systems Laboratories (NTT-IIESL). I am very grateful to Dr. Nobuo Inagaki, President of AFTEX Co. Ltd. (former Executive Director of NTT-IRL), Dr. Tomoyuki Toshima, President of NTT Intelligent Technology Co. Ltd. (former Executive Director of NTT-IRL and NTT-IIESL), Dr. Masataka Hirai, Executive Director of NTT-IIESL, Dr. Shigenobu Sakai, Executive Manager of Information Hardware Systems Laboratories of NTT-IIESL, and Dr. Tadashi Katoh, Supervisor of Sensing Systems Research Group of NTT-IIESL for their support and encouragement of this work.

List of Author's Publications

[1] M. Hirano and K. Shinjo: "Atomistic locking and friction" *Physical Review* **B41**, 17, 11837-11851 (1990).

[2] K. Shinjo and M. Hirano: "Dynamics of friction: superlubric state" *Surface Science* **283**, 473-478 (1993).

[3] M. Hirano and K. Shinjo: "Superlubricity and frictional anisotropy" *Wear* **168**, 121-125 (1993).

[4] M. Hirano, K. Shinjo, R. Kaneko, and Y. Murata: "Anisotropy of frictional forces in muscovite mica" *Physical Review Letters* **67**, 2642-2645 (1991).

[5] M. Hirano, K. Shinjo, R. Kaneko, and Y. Murata: "Observation of superlubricity by scanning tunneling microscopy" *Physical Review Letters* **78**, 1448-1451 (1997).

[6] M. Hirano and K. Shinjo: "Atomistic origin of friction" *Proceedings of the Japan International Tribology Conference, Nagoya, October 1990*, 1207-1212 (1990).

[7] M. Hirano and K. Shinjo: "Superlubricity: a state of vanishing friction" in *Computer Aided innovation of New Materials II*, edited by M. Doyama, J. Kihara, M. Tanaka, and R. Yamamoto (Elsevier Science Publishers B. V., Amsterdam, 1993) 537-542 (1993).

[8] M. Hirano and K. Shinjo: "Superlubricity: solid-solid surface interaction analysis by molecular dynamics" *Proceedings of the International Conference on Computer-Assisted Materials Design and Process Simulation, Tokyo, September 1993*, 207-212 (1993).

[9] 平野元久, 新上和正, 金子礼三: "摩擦の研究" *NTT R&D* **40**, 6, 869-876 (1991).

[10] 新上和正, 平野元久: "摩擦の研究" 物性研究 **55**, 6, 577-602 (1991).

[11] 平野元久: "超潤滑" 数理科学 **364**, 23-28 (1993).

[12] 平野元久, 新上和正: "超潤滑: 摩擦の無い状態" 応用数理 **4**, 1, 13-29 (1994).

[13] 平野元久, 新上和正: "超潤滑" 機械の研究 **46**, 1, 197-200 (1994).

[14] 平野元久, 新上和正: "摩擦の起源: 超潤滑" トライボロジスト **39**, 5, 393-400 (1994).

[15] 平野元久: "超潤滑" 自動車技術 **48**, 12, 36-37 (1994).

Contents

List of Figures

Chapter 1

Introduction

When two solid bodies contact each other and one body subsequently slides against the other, friction occurs [1, 2, 3, 4, 5, 7]. Enormous amounts of experimental data have shown that energy, i.e., frictional energy is necessary for sliding contacting bodies. This indicates that there is a force (friction force) parallel to the contacting surfaces.

Several models (or views) have been proposed to explain the origin of this friction force[1] . Some relate to the mechanical locking of surface asperities [8], and others to the atomistic origin, i.e., the molecular interactions between the constituent atoms of solids [9, 10]. Problems of friction in real systems can be solved from the viewpoint of phenomenology by a priori assuming that a friction force exists [6, 11, 12]. In real systems the measured data usually contains many unknown factors: surface roughness and poisoning by contaminants such as O_2, H_2, and oil. It is difficult, therefore, to study the origin of the friction force from the experimental data available at present.

More recent experimental studies [13, 14], however, excluded many of the unknown factors by preparing well-defined surfaces. The purity and completion of such surfaces can be detected by current surface analysis techniques such as scanning tunneling microscopy (STM) [15, 16] and atomic force microscopy [17]. New technology developed by groups at IBM [13] and the University of Basel [18] has made possible the measurement of friction even at atomic-scale resolution. On the practical front, also, friction is an important issue for future technologies such as micromachines [19].

The purpose of thesis is to study the origin of the appearance of friction from the atomistic point of view. Two experiments show that friction forces of clean surfaces greatly depend on the atomic arrangements of contacting surfaces. In the first experiment, the friction forces of single-crystal muscovite mica are measured as a function of the lattice misfit between the two contacting cleavage surfaces at a very light load under both dry and ambient atmospheres [20]. The measured friction forces are anisotropic with respect to the lattice misfit. They increase (decrease) when the surfaces contact without (with) lattice misfit. The underlying mechanisms of the anisotropy are discussed by considering the effects of interface atomic arrangements, which are theoretically examined in the latter half of this thesis. The second experiment demonstrates the effects of interface atomic arrangements by using atomically clean and well-defined surfaces [21, 22]. The friction forces of the

[1] The first scientific descriptions of frictional properties of materials appeared in the Italian Renaissance. Leonardo da Vinci studied solid sliding friction, and discovered the rules of sliding friction.

atomically clean surfaces of Si(001) and W(011) are measured under ultra-high vacuum by scanning tunneling microscopy. The surfaces are slid against each other while the tunneling gap between them is controlled. This enables the surfaces to slide in elastic contact on the atomic scale. The measured friction forces also exhibit anisotropy with the lattice misfit of the contacting surfaces. The magnitude of the friction force is comparable to theoretical values. The experiments also show that the friction force can be very small, below the detection limit, at misfit contact conditions. These two experimental results agree with theoretical predictions.

The latter half of this thesis theoretically studies the atomistic origin of the friction force intrinsically generated by the molecular interactions between the constituent atoms of solids [23, 24]. It is shown that there are two origins: *atomistic locking* and *dynamic locking* [23]. Atomistic locking occurs when the configuration of atoms on a contact surface continuously changes with the sliding distance and when the interatomic potentials have an arbitrary strength. In contrast, dynamic locking occurs when the configuration changes discontinuously due to the dynamic process and if the interatomic potential is stronger than a specific given value. A criterion is derived for the occurrence of dynamic locking. From studies of various systems, it can be seen that dynamic locking is unlikely to occur in realistic systems. The friction forces due to atomistic locking are calculated for α-iron. One other important finding is that certain unique cases exist where friction force exactly vanishes if completely clean solid surfaces are prepared.

Dynamics in friction has also been theoretically studied from an atomistic point of view [24]. Friction is formulated as a problem of whether or not a given kinetic energy for the translational motion dissipates into the kinetic energies for the internal motions during sliding. From a study of the Frenkel-Kontorova model with kinetic energy terms, it is found that two different regimes appear in the parameter space specifying the model: the superlubricity and the friction regimes. Friction completely vanishes in the superlubricity regime and appears in the friction regime. The conditions for superlubricity to occur are described. It is emphasized that a high dimensionality in the friction system is a key to understanding the physics of superlubricity. For high-dimensional systems, superlubricity is a generic phenomenon, appearing for a wide class of (strong or weak) adhesion such as metallic bonding and the Van der Waals interaction. The problem of what triggers the friction is studied by examining the available phase space volume in dynamics. Friction is discussed, in relation to the mixing property in the dynamics for the internal motions.

The organization of this thesis is as follows: Chapter 2 presents observations of the anisotropy of friction forces with the atomic arrangements of contacting surfaces in single-crystal muscovite mica, and discusses the underlying mechanisms of the anisotropy in connection with the theory presented in Chapter 4, explaining the effects of interface atomic arrangements on friction. Chapter 3 confirms the effects of interface atomic arrangements by examining the sliding systems of atomically clean surfaces by using ultra-high vacuum scanning tunneling microscopy. Chapter 4 provides the theoretical background of the experiments presented in Chapters 2 and 3. It is shown how friction appears from the molecular interactions, depending on interface atomic arrangements. Chapter 5 theoretically studies the dynamics of friction from an atomistic point of view, and explains how the energy is dissipated in dynamic friction.

Chapter 2

The Anisotropy of Friction Forces in Muscovite Mica

2.1 Introduction

The frictional properties of various single crystals have been measured, and it has been shown that the friction forces of some single crystals are anisotropic with respect to the crystallographic direction of sliding [25, 26, 27, 28, 29]. For example, when sliding the {001} planes of a single-crystal diamond against another in air, the frictional force is smaller for sliding in the <110> direction than in the <100> direction by a factor of 2/3 [25]. The clean surfaces of some hexagonal metals showed the anisotropy, in which the friction force of the {0001} planes in the $<11\bar{2}0>$ direction was smaller than that of the $\{10\bar{1}0\}$ planes in the $<11\bar{2}0>$ direction by a factor of 1/2, when sliding single-crystal cobalt against polycrystalline cobalt [26]. Some other materials such as copper [27, 28] and ceramics [29]. also showed frictional anisotropy, depending on the crystallographic direction of sliding.

Plastic deformations and fractures were observed at the rubbed surfaces when the anisotropy appeared in the above systems, and the mechanisms of the observed anisotropy were analyzed by examining the preferred slip system in single crystals. The anisotropy of diamond was interpreted by the preferred slip system in which <110> sliding is more likely than <100> sliding to yield the critical resolved shear stress that activates the lattice slip and the subsequent crack formation on the primary slip plane, which was assumed to be {111} [25]. The anisotropy disappeared at very small loads, i.e., when the contact condition approached being elastic below the determined critical mean contact pressure [25].

This chapter reports the first observation of frictional anisotropy in muscovite mica by measuring the friction forces at very small load as a function of the lattice misfit angle between the two contacting lattices. The underlying mechanisms of the observed frictional anisotropy are examined in connection with the theoretical conclusion[23] on the effects of the commensurability between contacting lattices. It is shown that the frictional forces are anisotropic with respect to the lattice misfit angle, i.e., they increase (decrease) when the contacting surfaces approach being commensurate (incommensurate). From studying how introducing dirtiness into the contacting surfaces affects the friction forces and from measuring the highly-resolved surface roughness of the mica cleavage surfaces, it is concluded that the observed anisotropy stems from the change in commensurability of contacting

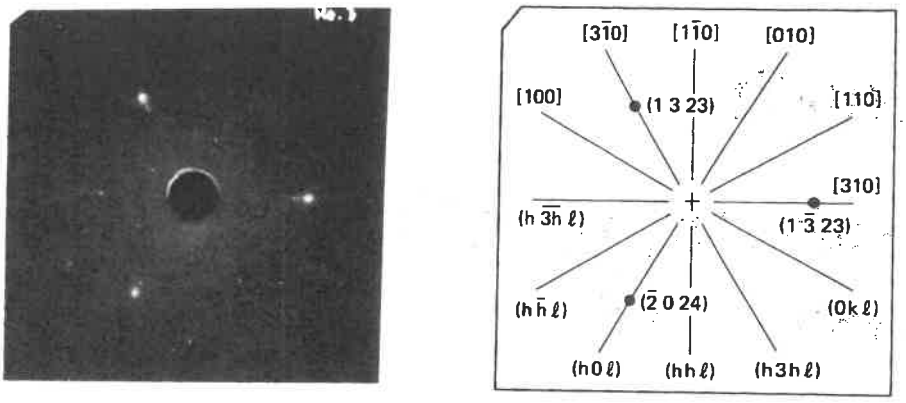

Figure 2.1: (a) Back-reflection Laue pattern of muscovite mica. (b) Map showing lines made by a set of reciprocal points of zone planes. The angles between zone axes [010] and [110], and between [010] and [310], are respectively 29.89 degrees and 59.89 degrees. The representative diffraction spots are identified as (1 3 23), (1 $\bar{3}$ 23), and ($\bar{2}$ 0 24). The high intensities are due to satisfying the first-order diffraction condition.

lattices.

2.2 Experimental

Muscovite mica is suitable for my purpose since it is a relatively large single crystal and its cleavage surface has few steps, being atomically flat. Mica surfaces have been successfully used for measuring friction forces [30] and adhesive forces [31, 32]. The lattice orientations were determined by X-ray diffraction prior to friction testing. X-ray diffractometer experiments confirmed that mica has a monoclinic structure, whose space group is C_{2h}^6 [33]. Figure 2.1 (a) shows the back-reflection Laue pattern of the mica in approximately the [001] direction. Figure 2.1(b) shows the corresponding map representing lines made by a set of reciprocal lattice points of zone planes, denoted (hkl), belonging to the zone axes, denoted [hkl]. Several of these patterns were examined at different points over a 1-cm^2 area on the sample. The Laue patterns were nearly invariant at the different points, implying that the mica used is a relatively large single-crystal over the 1-cm^2 area. The lattice orientation of the cleavage surface was determined by specifying the primitive vector **b** perpendicular to the line made by a set of reciprocal points of zone planes belonging to the zone axis denoted [010] in the map shown in Fig. 2.1(b).

Figure 2.2 shows the schematic set-up for the measurement. Two mica sheets were cut from a larger sheet as carefully as possible to make the edges of the mica sheets smooth. One sheet was attached to a cylindrically curved substrate with an 8-mm radius and 5-mm length (upper specimen); the other to a disk substrate with a 10-mm diameter (lower

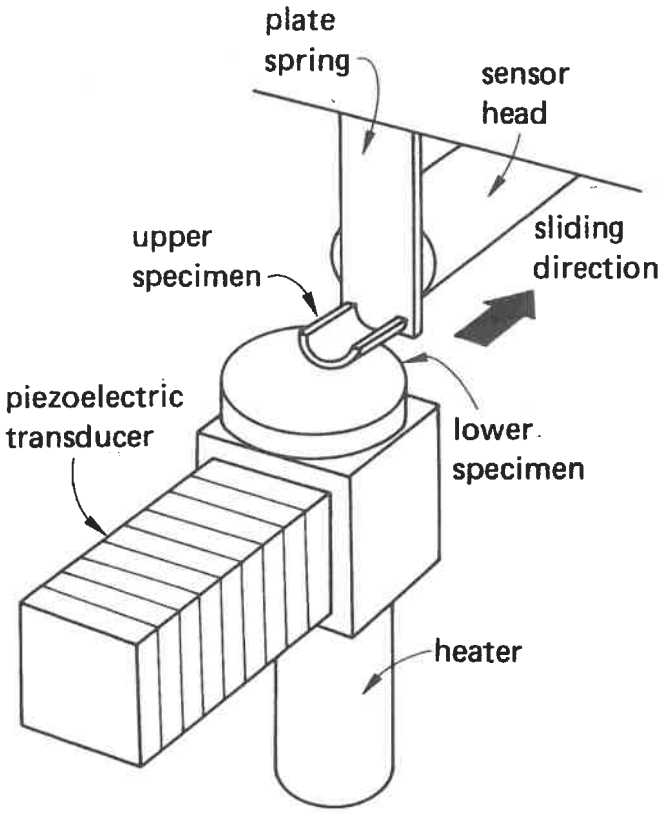

Figure 2.2: Schematic illustration of friction-measuring apparatus. The sliding direction is shown by the arrow corresponding to the direction of extension of the piezoelectric transducer. Movement per unit voltage of the piezoelectric transducer is 0.18 μm/V. The resolution of the measured friction force is estimated to be 1×10^{-6} N according to the 0.1-μm spatial resolution of the capacitance displacement meter.

specimen). Friction was measured under an argon-purged dry atmosphere with controlled water vapor pressure and at a raised surface temperature (over 100 degrees) to reduce the thickness of contaminants such as water and organic compounds on the cleavage surfaces. The surface temperature was determined using a radiation thermometer to measure the temperature of a black tape, whose emissivity is approximately 1.0, stuck onto the mica cleavage surface. The mica sheets were cleaved again after finally attaining the lowest water vapor pressure in the chamber. The upper specimen was then placed on the lower specimen at a load corresponding to its own weight (1.2×10^{-3} N); this gave an elastic contact zone of 0.25 μm by 5 mm and a mean contact pressure of 0.9 MPa according to the measured elastic constants [34].

Static and dynamic friction forces were measured between the two contacting specimens during one traverse of a few μm. First, both the upper and lower specimens were moved by extending the piezoelectric transducer at a speed of 2.7 μm/s toward the thin plate spring

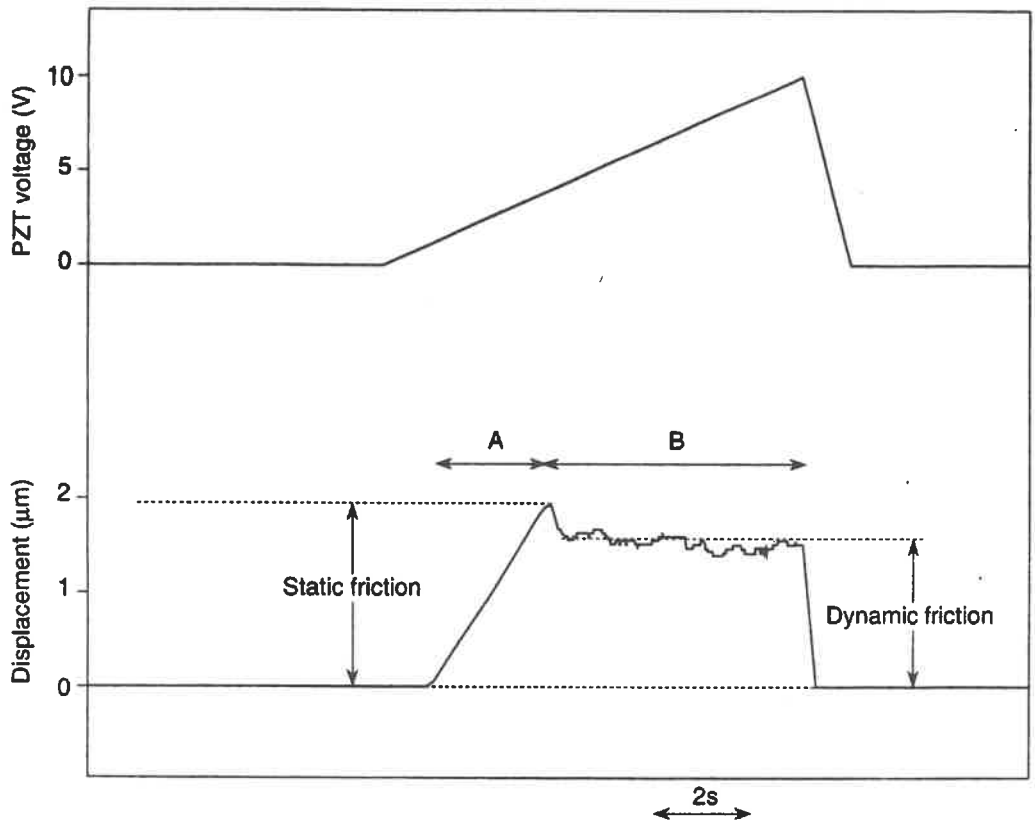

Figure 2.3: The voltage applied to piezoelectric transducer (upper curve) and the the displacement of the plate spring during sliding of mica surfaces (lower curve).

($5 \times 15 \times 0.1$ mm^3), whose spring constant is 30.6 N/m. As the two specimens approached the plate spring, only the upper specimen touched the spring. The deflection of the spring was monitored using a displacement meter to detect the change in capacitance between the plate spring and the displacement meter sensor head. When the spring force overcame the friction force, sliding occurred. The spring force during sliding determined the static and dynamic friction forces.

The typical measured data are shown in Fig. 2.3. The upper curve shows the voltage applied to piezoelectric transducer, and the lower curve shows the displacement of the plate spring. Region A indicates pre-sliding before the onset of sliding. The maximum displacement obtained at the onset of sliding gives static friction force. Dynamic friction force is obtained from the averaged displacement of the plate spring after the the onset of sliding at the sliding region B.

2.3 Results and discussion

The change in the measured static and dynamic friction forces with the lattice misfit angle θ, the angle between the two contacting mica lattices, is shown in Fig. 2.4. The two specimens were brought into contact such that each primitive vector **a** corresponded to the sliding direction shown in Fig. 2.4. In a dry atmosphere with a relative water

vapor pressure $p/p_0 \sim 9 \times 10^{-5}$ and at a surface temperature of 130 degrees, the static and dynamic friction forces show the anisotropy in which the friction forces increase as the misfit angle approaches $\theta = 0$ degree or 60 degrees, and decrease as it approaches $\theta =$ 30 degrees. Alternatively, they increase (decrease) when the contacting surfaces approach being commensurate (incommensurate). The static friction force ranges from 2.2 to 7.6 $\times$ 10^{-4} N. The changes in the friction forces seem to have sixfold symmetry, reflecting the pseudo-hexagonal symmetry of the cleavage surfaces, which are defined as the potassium layer sandwiched between the two hexagonal sheets of silicate tetrahedra. The measured atomic parameters showed the mica structure to be slightly distorted from the ideal structure by a departure from hexagonal symmetry on the surface of the silicate sheets [35]. However, no frictional anisotropy can be seen in the ambient atmosphere in Fig. 2.4. This can be due to the introduction of dirtiness (water) to the contacting surfaces. McGuiggan et al. [31] observed the anisotropy of the adhesion energy between two contacting mica cleavage surfaces in distilled water and in aqueous KCl. The results showed the adhesion peaks at specific angles corresponding to crystallographic atomic alignment (θ=0 , 60, 120, and 180 degrees). However, their observation cannot be directly related to the observed anisotropy because of the different atmosphere where the measurements were done. Their results were explained by the excess surface energy of a low-angle grain boundary. On the other hand, they observed no anisotropy of adhesion energy in an N_2 environment at a relative humidity of 33%, corresponding to the results showing no frictional anisotropy in ambient air.

The static friction forces are shown in Fig. 2.5 as a function of the twist angle between the two contacting specimens with different relative water vapor pressures and at different surface temperatures. Here, the lattice orientations of the upper and lower specimens were measured, but not specified with respect to the sliding direction, i.e., each primitive vector **a** does not necessarily correspond to the sliding direction, while the lattice orientation of both surfaces were initially matched at the twist angle θ_l=0 degree. Figure 2.5 the anisotropy of the static friction force, which ranges from 2.5 to 5.0 $\times$ 10^{-4} N over θ_l=0 to 90 degrees under a dry atmosphere and at a high surface temperature. The average thickness of the water layer adsorbed on the mica cleavage surfaces can be less than a few Å, i.e., the cleavage surfaces are clean, under an extremely low relative water vapor pressure p/p_0 of 9 $\times$ 10^{-5}, according to the measurement made on a cleavage surface of lithium fluoride using ellipsometry, in which the average water layer thickness was negligibly small below $p/p_0 \sim$ 0.3 [36]. By increasing the relative water vapor pressure and subsequently decreasing the surface temperature, it is seen in Fig. 2.5 that the anisotropy gradually weakens, and then disappears under an ambient atmosphere.

The mean contact pressure of 0.9 MPa at the mica contacting surfaces is three orders smaller than the values of 0.4 GPa at cobalt surfaces [26] and 0.3 GPa at copper surfaces [27, 28]. This suggests that the contact condition of the mica might be elastic if one takes into consideration that the elastic constant c_{44} of 12 GPa for mica is comparable in magnitude to that of 75 GPa for cobalt and copper. The topographies of the contacting surfaces were measured before and after sliding by both an atomic force microscope (AFM) [17] over a 5-nm by 5-nm scan and by a point contact microscope (PCM) [37] over a 2000-nm by 2000-nm scan. The as-cleaved mica surfaces were flat on an atomic scale, within 0.2-nm resolution, according to the AFM measurements in repulsive mode. The atomically-resolved

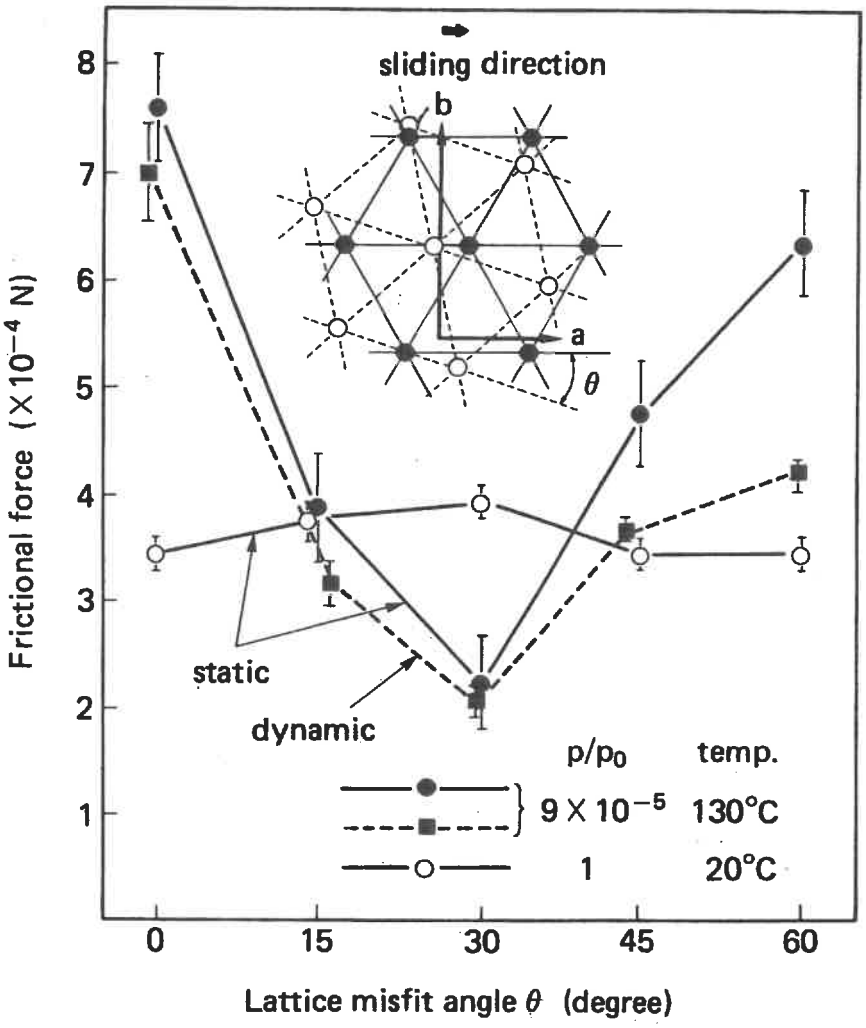

Figure 2.4: The change in the measured static and dynamic friction forces as a function of the lattice misfit angle θ between two contacting mica lattices. The misfit angle is approximately 0 degree when the two specimens are brought into commensurate contact without rotation of the lower specimen.

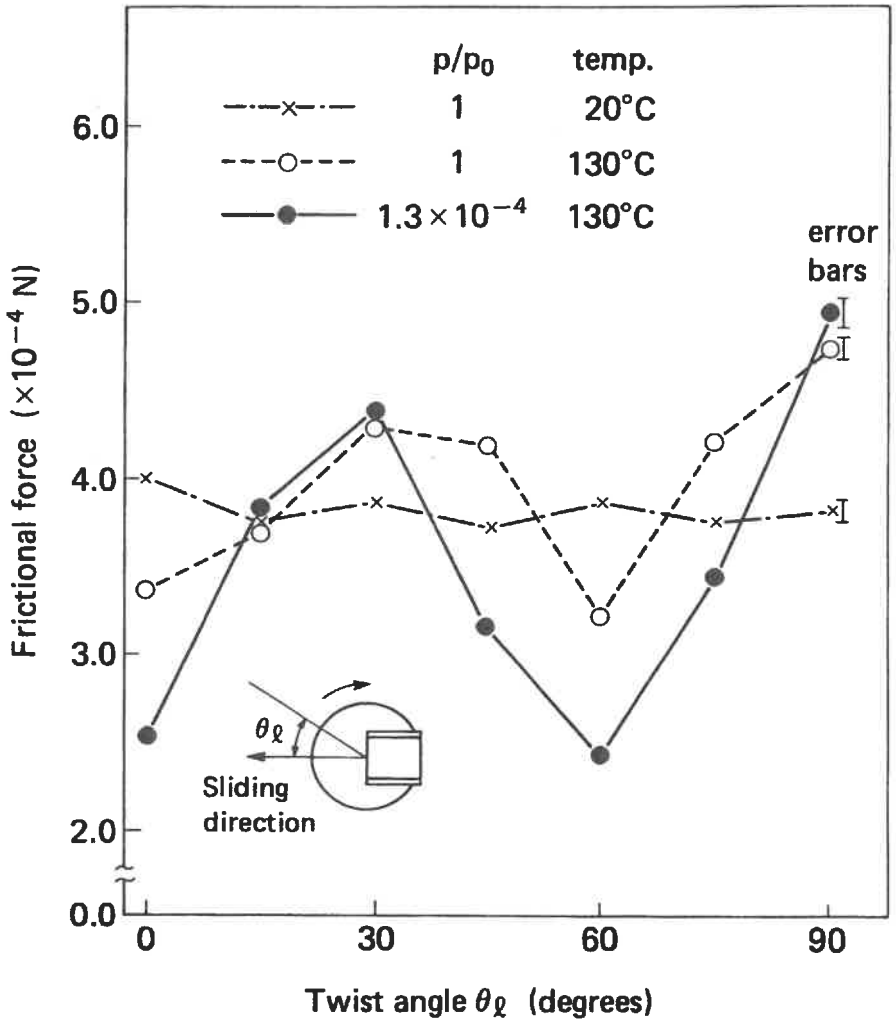

Figure 2.5: The change in the measured static friction force as a function of twist angle θ_l between the two contacting specimens.

periodic variation in the surface force were obtained by scanning a sharp silicon nitride tip [38]. The PCM images showed no topographical changes, within a 2-nm resolution, between before and after sliding. Thus appreciable plastic deformations and fractures were unlikely to occur at the sliding mica surfaces. This implies that the contact condition of mica is elastic, which is different from the plastic contact in the previously observed frictional anisotropy [25, 26, 27, 28, 29].

It was shown that the static and dynamic friction forces between contacting mica cleavage surfaces increase when the surfaces approach being commensurate, and decrease when incommensurate. In Chapter 4 [23], new mechanisms for the atomistic origin of static and dynamic friction forces is proposed by theoretically studying a three-dimensional many-particle system, in which clean and flat surfaces contact elastically. My picture explained how the static friction force appears in terms of interatomic potentials and atomic configurations of surfaces, and how the given translational energy of a sliding body is dissipated in dynamic friction. It was concluded that the friction force appears when contacting surfaces are commensurate, and that they vanish, when incommensurate. Therefore, the observed frictional anisotropy in mica is consistent with the theoretical conclusion [23]. Erlandsson et al. [30] observed the atomic-scale periodic change in the friction forces of mica by scanning a polycrystalline tungsten sharp tip on a mica cleavage surface. They also remarked on the potential importance of the commensurability of contacting surfaces as a cause of their observed periodic change.

The frictionless state has been discussed for the case of weak interfacial interactions such as Van der Waals interaction [39, 40, 41, 42, 43, 44]. The criterion for the occurrence of the frictionless state is derived in a three-dimensional many-particle system [23]. The threshold of interfacial interaction strength for which friction forces vanish were determined for cubic metals [23]. Consequently, it has been concluded that frictionless state appears for a wider class of interfacial potentials including strong interactions such as metallic bonding, i.e., the state of *superlubricity* exists in realistic systems [23, 45, 46, 47].

It is clear from Fig. 2.5 that the friction forces become small as surfaces are cleaned when contacting incommensurately. It is then expected to observe much smaller friction forces by preparing more well-defined surfaces. However, the observed lowest friction force at $\theta = 30$ degrees (when incommensurate) shown in Fig. 2.4 is not so small. This might be due to some deviation from perfect cleanliness and perfect periodicity over the contacting area. Experiments using the well-defined surfaces under a high vacuum of 10^{-11} Torr will be reported in future.

2.4 Conclusion

The friction forces of muscovite mica were measured as a function of the lattice misfit angle between the two contacting cleavage lattices, and it was found that the friction forces are anisotropic with respect to the lattice misfit angle, i.e., they increase (decrease) when the surfaces approach being commensurate (incommensurate). The observed frictional anisotropy stems from the change in the commensurability between contacting lattices as predicted by the theory [23].

Chapter 3

Frictional Anisotropy in Atomically Clean Surfaces

3.1 Introduction

In the previous chapter, the frictional anisotropy, in which the friction forces on cleaved mica surfaces increase (decrease) when surfaces contact without (with) the lattice misfit along sliding direction, was observed. Martin *et al.* [49] found an ultra-low friction coefficient (below 10^{-3}) in MoS_2 polycrystal films having the lattice misfit between the basal planes in the grain. They attributed it to the friction-induced lattice orientation change of an intercrystallite slip system, in which the basal planes were aligned in the sliding direction and disordered around the c-axis.

The purpose of this experiment is to find experimental evidence for the frictional anisotropy on interface lattice misfit in atomically clean surfaces by using ultra-high-vacuum scanning tunneling microscopy (UHV-STM) [21, 22]. To do this, friction forces are measured when sliding the atomically clean surfaces of Si(001) and W(011) by changing the lattice misfit between them. It is shown that friction was not observed when the surfaces contact with lattice misfit along sliding direction in measurements capable of resolving a friction force of 3×10^{-9} N, whereas friction with a magnitude of 8×10^{-8} N, which is comparable to theoretical values, was observed when the surfaces contact without lattice misfit along sliding direction.

In this chapter, the friction forces of atomically clean surfaces are measured by using UHV-STM [21]. This method is used because it achieves "sliding in elastic contact" between atomically clean surfaces by utilizing the tunneling between the surface of the tip of a probe wire and the surface of a single crystal. Therefore, plastic deformation does not occur at sliding interfaces, as it does with conventional friction testing when surface asperities interact with each other under the application of a certain amount of load normal to surfaces. Here the friction between the surfaces is measured rather than the adhesion between them, as was done in previous STM studies [50, 51].

3.2 Experimental

In the present system, a clean Si(001) (n-type, 0.01 Ω·cm) surface was one-dimensionally scanned against a clean W(011) surface at the tip of a polycrystalline tungsten wire (inset, Fig. 3.1) using a piezoelectric tube scanner. The tunneling gap between the W(011) surface at the tungsten tip and the Si(001) surface was controlled by adjusting the tunneling parameters. The scanning was conducted under weak feedback control, i.e., it was done at an almost constant height.

The area of the W(011) surface, i.e., the interaction area of contact, was estimated to be a few nanometers square based on the observations of the tip with a scanning electron microscope (SEM), the same method as used by Kuroda *et al.* to observe a W(011) surface and other various crystal planes located near the tip [52]. The tungsten wire was also used as a flexible cantilever beam to probe the friction force between the W(011) and Si(001) surfaces. This force was determined by measuring the deflection of the beam using a focusing-error-detection optical displacement sensor [53] with a resolution of 2 nm. The friction forces to be measured were on the order of 10^{-7} N in the friction regime, based on calculated values [23]. Prior to scanning, the lattice misfit along sliding direction is measured between the W(011) and Si(001) surfaces, by rotating the tungsten wire around its longitudinal axis (Fig. 3.1). Theoretical predictions indicated that friction highly depends on the the lattice misfit along sliding direction, as will be seen in Chapter 4. It is then examined how the measured friction forces changed with the lattice misfit between the W(011) and Si(001) surfaces. The lattice orientation and cleanliness of the surfaces were determined by field electron microscopy (FEM) for the W(011) of the tip, and by low-energy electron diffraction (LEED) and Auger electron spectroscopy (AES) for the Si(001). The silicon sample was moved into appropriate position for it to be cleaned and for LEED and AES measurements to be performed on it. The tungsten tip faced the silicon sample during friction measurements and faced a microchannel plate during FEM measurements. Since foreign gaseous elements in UHV are likely to stick to fresh tungsten surfaces, the friction measurements was done within about ten minutes after cleaning the tip. This time limit was determined by examining the degradation of FEM images with time in UHV.

The flat W(011) surface was made at the tungsten tip by heating (flashing) the tip to over 2300 K in a UHV environment by electron bombardment. The radius of the tip is around 20 nanometers based on the SEM observation of the tip. The tip radius was also estimated from FEM measurements using Fowler-Northeim equation expresed by

$$\frac{I}{V^2} = a \exp\left(\frac{-b'\phi^{3/2}}{V}\right), \tag{3.1}$$

where I is the total current and

$$a = A6.2 \times 10^6 \left(\frac{\mu}{\phi}\right)^{\frac{1}{2}} (\mu + \phi)^{-1} (\alpha k r)^{-2}, \tag{3.2}$$

$$b' = 6.8 \times 10^7 \alpha k r. \tag{3.3}$$

In these equations A is the total emitting area, α the Nordheim image-correction term, and kr the field voltage proportionality factor. A plot of $\ln(I/V^2)$ versus $1/V$ is therefore linear with intercept $\ln a$ and slope $S = -b'\phi^{\frac{3}{2}}$. If α is taken to be unity and $k \cong 5$, a value

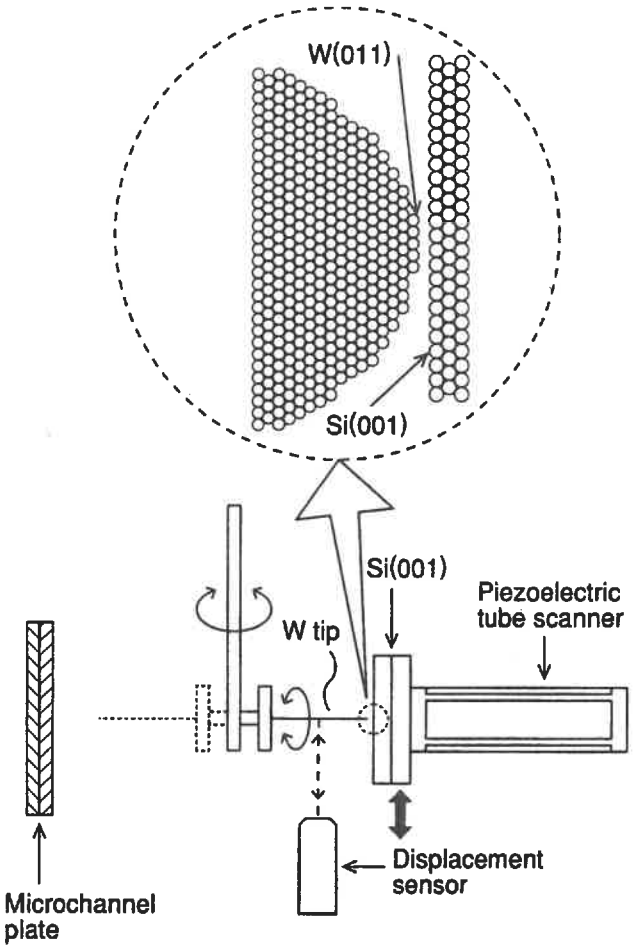

Figure 3.1: Schematic illustration of the UHV-STM friction measurement system in an ultra-high vacuum with a base pressure of 10^{-11} torr. The inset shows an atomic illustration of the tip and surface. The measurement system was placed on a vibration isolation air platform, which had a resonance at 1.2 Hz.

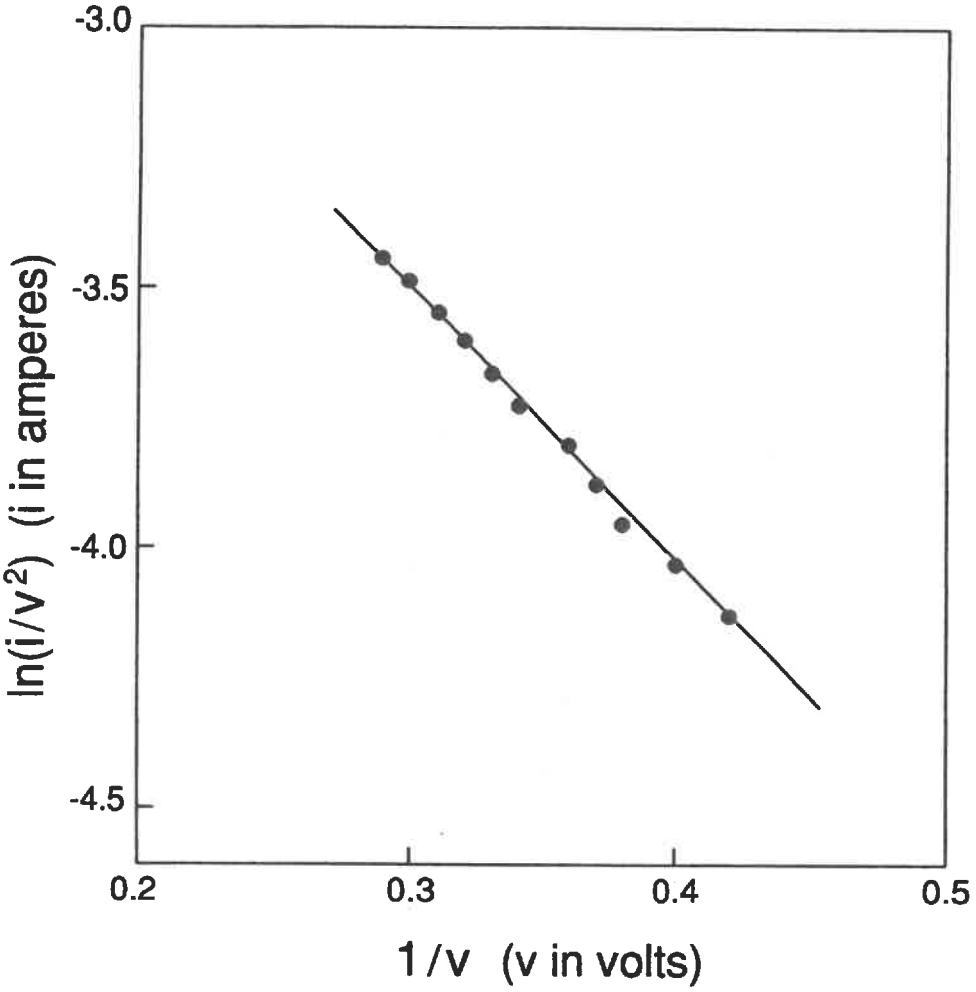

Figure 3.2: Fowler-Northeim plot, showing a plot of $\ln(I/V^2)$ versus $1/V$.

of r, correct to within 20 percent, can be found at once from S if ϕ is known and uniform. From the plot of $\ln(I/V^2)$ versus $1/V$, shown in Fig. 3.2, the tip radius r is estimated to be around 20 nanometers.

The tungsten tip was fabricated by electrochemically etching a polycrystalline tungsten wire with a diameter of 0.25 mm. The side wall of the tungsten wire was also electrochemically etched to increase the reflectivity of the laser light (λ=780 nm) from the optical displacement sensor. The final diameter was 0.20 mm. The wire was made 40 mm long to make it flexible enough to allow us to measure the wire deflection caused by friction. The spring constant of the wire was set at 1.5 N/m. Prior to etching, the wire was straightened by stretching it in a hot atmosphere. The straight wire could be set perpendicularly within one degree to the Si(001) surface by careful mechanical alignment. The FEM image shown in Fig. 3.3 (a) is a typical image of a clean tungsten tip, as previously observed by Müller [55]. The image reflects differences in the work function of the crystal planes located at the tip, and this determines the lattice orientation of the W(011), shown in Fig. 3.3 (b). The dark area at the center of the FEM image represents the W(011) because it has a high

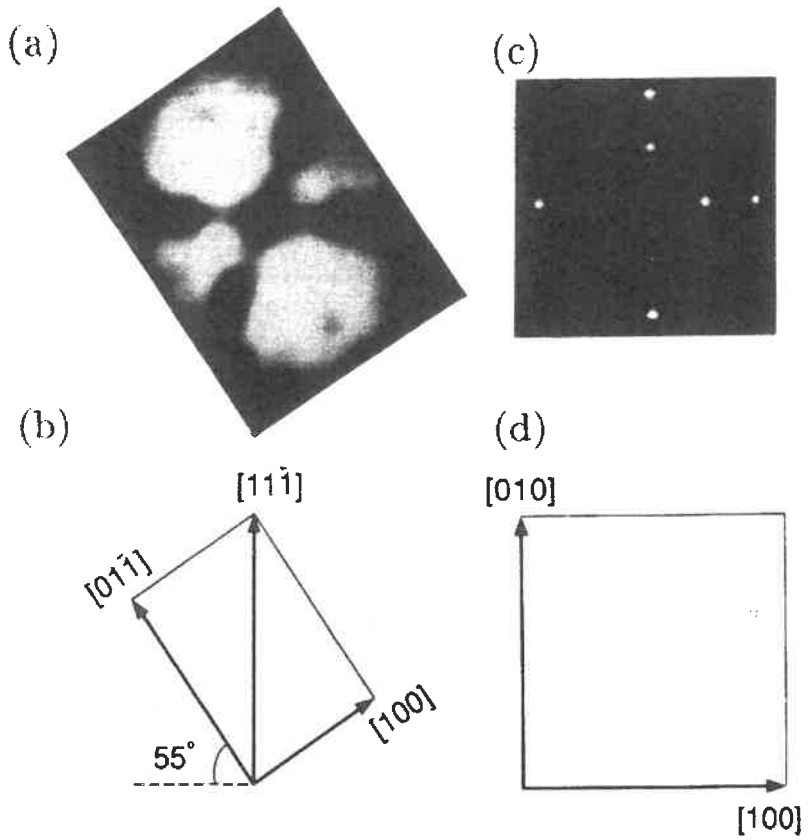

Figure 3.3: (a) FEM image of a clean tungsten tip. (b) lattice orientation of W(011). (c) LEED pattern of clean Si(001). (d) lattice orientation of Si(001).

work function; its area was roughly estimated to be a few nanometers square from simple geometrical calculations.

Clean Si(001) surfaces were obtained as follows. A carbon-free SiO_2 film was formed on a silicon wafer by immersing the wafer into several solutions [56]; the film was then removed by heating the wafer at 1173 K for one hour in UHV by electron bombardment. Clear (2×1) LEED patterns, as shown in Fig. 3.3 (c), were routinely obtained. The AES measurements showed the typical spectra for clean silicon and no carbon spectra on the Si(001) surface.

Fortunately, the contact without lattice misfit along a sliding direction between W(011) and Si(001) is obtained by appropriately aligning the lattice orientations of their surfaces (Figs. 3.3 (b) and (d)) in such a way that the [11$\bar{1}$] direction of the W(011) corresponds to the [010] direction of the Si(001). The ratio between the lattice unit along the [11$\bar{1}$] direction of the W(011) and that along the [010] direction of the (2×1) superstructure of Si(001) becomes rational in this alignment. The contact with lattice misfit along sliding direction, on the other hand, is easily obtained at arbitrary lattice misfits.

3.3 Results and discussion

The friction that occurred between W(011) and Si(001) surfaces was measured when they came into contact with and without the lattice misfit along sliding direction. Figure 3.4 shows the data obtained during scanning when the lattice orientations of the contacting surfaces were aligned without lattice misfit along sliding direction. The scanning amplitude was 100 nm and the scanning frequency was 0.5 Hz. The average tunneling current was maintained at the set value of 1 nA at a bias voltage of -100 mV applied to Si(001). The wire deflection signal oscillated with a period corresponding to that of the scanning, i.e., the wire was actually bent by the friction between the surfaces. The clear FEM image of the tip (Fig. 3.3 (a)) obtained after scanning shows that the tip was not damaged by the scanning and that sliding in elastic contact was achieved. The friction force was determined to be 8×10^{-8} N by multiplying the measured wire-bending deflection of 50 nm by the lateral spring constant of 1.5 N/m. The measured friction force is comparable to that calculated when sliding surfaces interact via short-range interfacial interactions [23].

Figure 3.5 shows the data obtained during scanning when the lattice orientations were aligned with lattice misfit along the sliding direction, in such a way that, for example, the $[01\bar{1}]$ direction of the W(011) corresponded to the [010] direction of the Si(001). The tunneling parameters, scanning amplitude, and scanning frequency were the same as those in the case without lattice misfit. The wire deflection signal was very different from that the case without lattice misfit. No oscillation of the wire deflection signal was observed in this measurement, which can resolve a wire deflection displacement of 2 nm. The corresponding friction measurement resolution was estimated to be 3×10^{-9} N. At the different tunneling parameters of -50 mV and 1 nA (Fig. 3.6(a)), and of -200 mV and 1 nA (Fig. 3.6(b)), no wire deflection oscillation was also observed. As in the case without lattice misfit, the tip was not damaged by scanning. Thus, no friction was observed at this friction-measurement resolution. Any wire deflection oscillation was not observed in any of the other contacts without lattice misfit.

The friction forces between W(011) and Si(001) surfaces were very sensitive to the tunneling gap. Figure 3.7 shows the wire deflection signals at two bias voltages (-100 and -900 mV) and at tunneling current of 1 nA. At -100 mV, under the contact without lattice misfit, using the same tip and Si(001) surface, the wire deflection signal oscillated, showing that friction occurred. Both dynamic and static friction occurred; the latter occurred when the tip stuck to the Si(001) surface.

The question is, what would happen when the bias voltage was decreased to -900 mV to cause the tip and Si(001) to separate. It was found that the oscillation disappeared even though the surfaces contact without lattice misfit along sliding direction. The gap increased by around 10 Å, as measured from the change in z-voltage applied to the tube scanner to control the gap. The tunneling gap was thus comparable to the interatomic distance at the tunneling parameters at which the upper curve was measured, and the interacting forces between W(011) and Si(001) were short-range.

The change in the gap caused by varying the bias voltage at a certain tunneling current was the same for both contacts with and without lattice misfit based on the measurement of z-voltage change at various bias voltages. For example, the gap decreased by around 2 Å when the bias voltage was increased from -100 to -50 mV, and it increased by around 3.5 Å when the bias voltage was decreased from -100 to -200 mV at a tunneling current of 1 nA

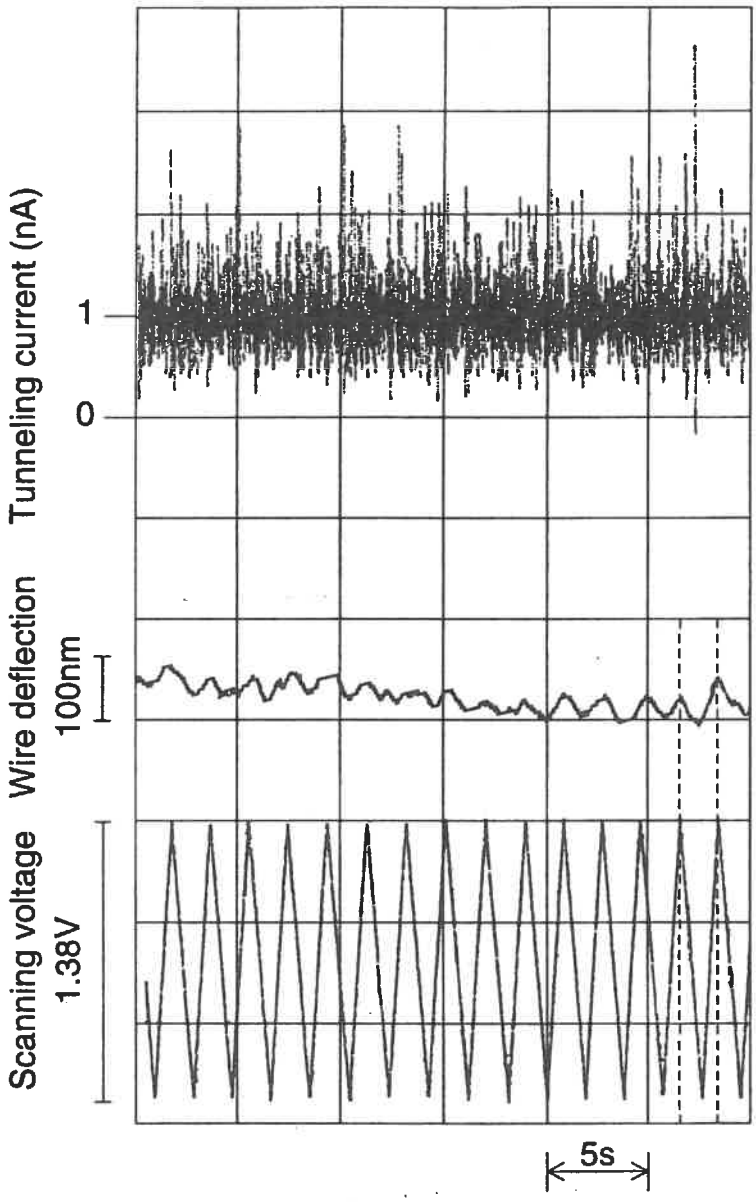

Figure 3.4: Scanning in no-lattice misfit contact conditions. This shows the tunneling current between the tungsten wire and the Si(001) surface, the deflection of the wire, and the scanning voltage applied to the piezoelectric tube scanner as a function of time.

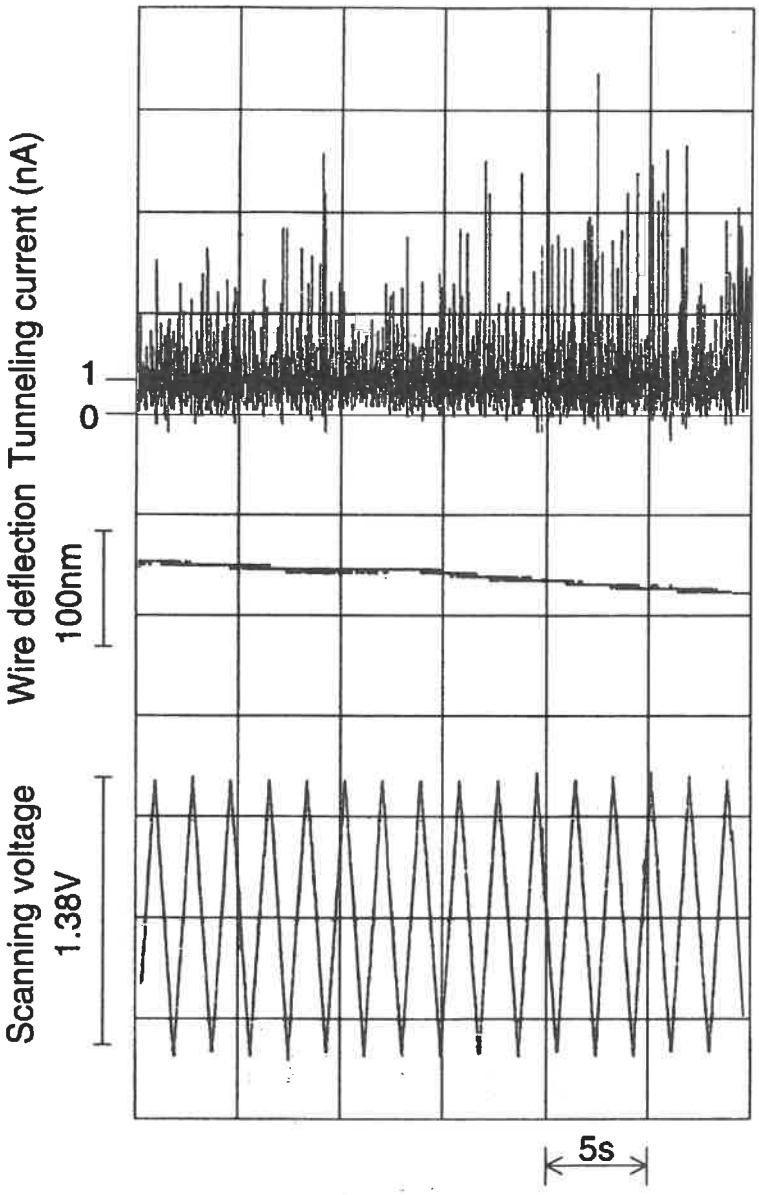

Figure 3.5: Scanning in lattice misfit contact conditions. This shows the tunneling current between the tungsten wire and the Si(001) surface and the deflection of the wire as a function of time (the scanning voltage was the same as in Fig. 3.4).

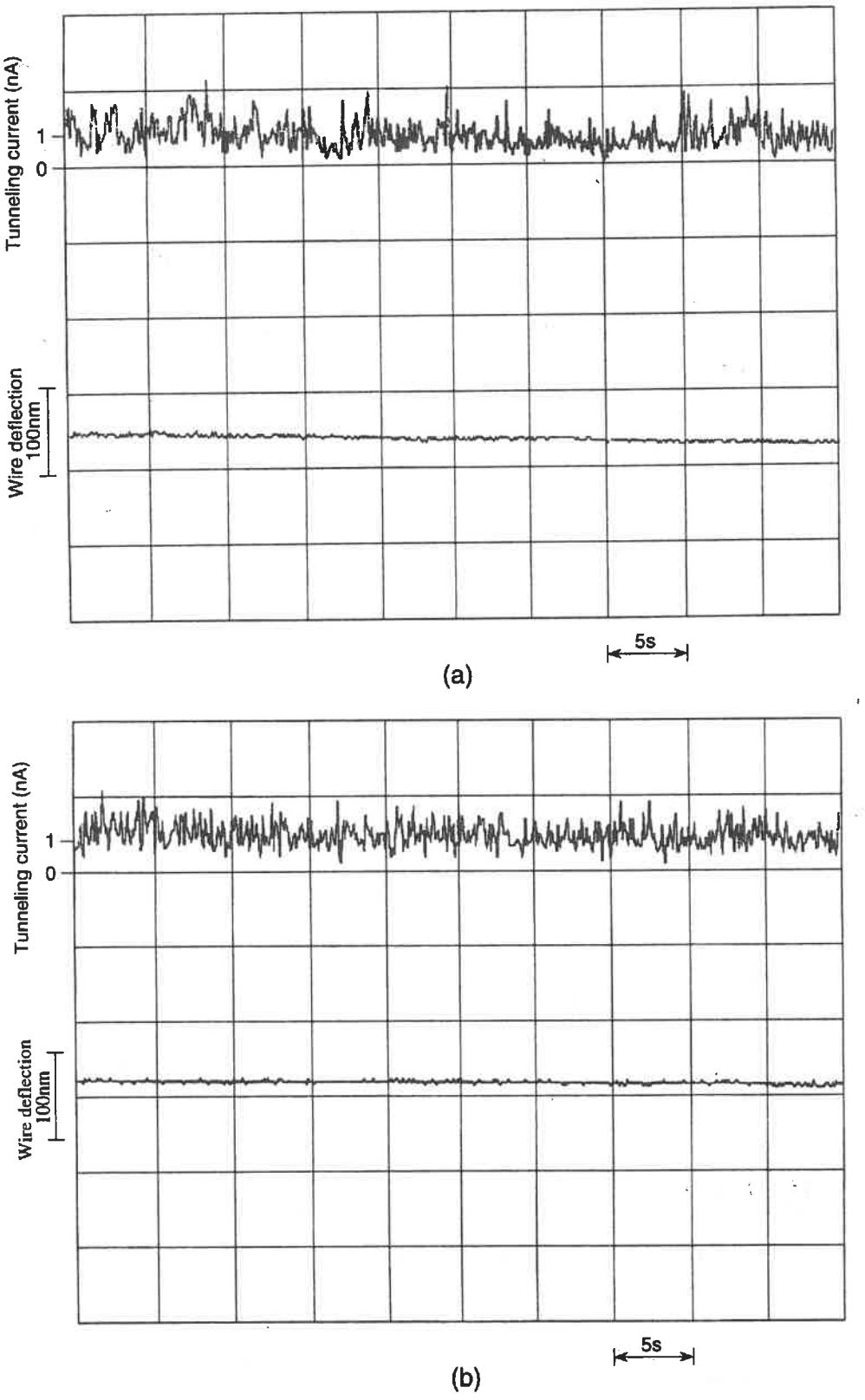

Figure 3.6: Scanning in lattice misfit contact conditions at the tunneling parameters of -50 mV and 1 nA (a), and of -200 mV and 1 nA (b).

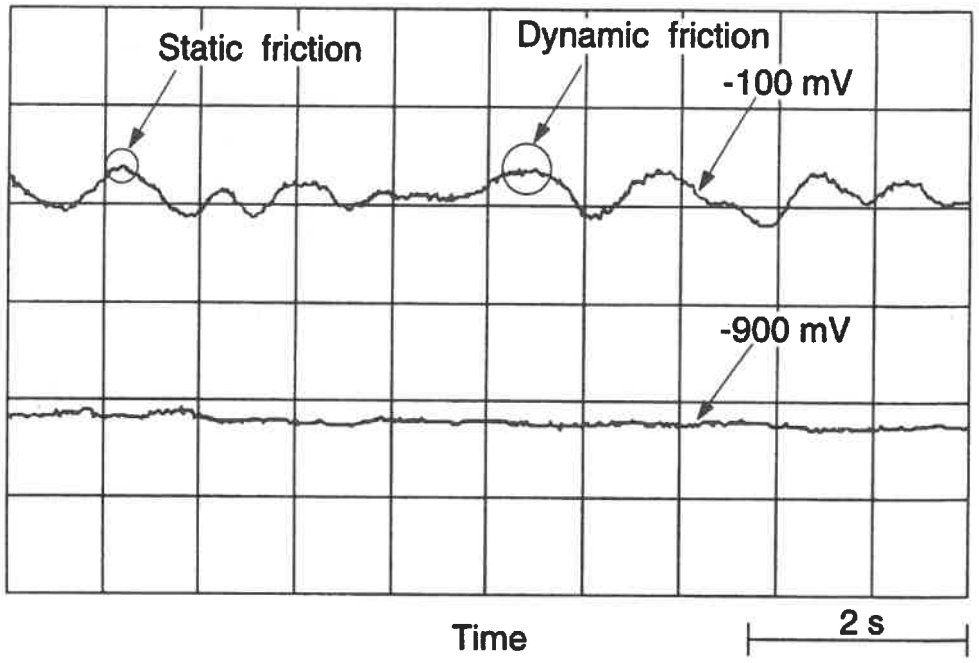

Figure 3.7: Dependence of tip-deflection signal on bias voltage applied to Si(001).

in both cases. Accordingly, the apparent tunneling barrier is the same for both of the cases with and without lattice misfit along sliding direction, showing that the distance between the W(011) and Si(001) surfaces can be set to the same value for both of the contacts with and without lattice misfit.

Theoretical studies showed that friction appearing between atomically flat crystal surfaces is irrelevant to a load applied normal to sliding surfaces because the energy barrier resisting a surface sliding a unit distance is unlikely to change when the normal load is changed by changing the interfacial distance. The calculations[54] actually showed that there exists a case in which friction completely vanishes even when strong adhesion operates under the application of force normal to sliding surfaces.

With the method presented here, it will be determined if the adhesive interaction is repulsive or attractive by simultaneously measuring the friction and adhesion by using a flexible wire that can bend horizontally and vertically.

3.4 Conclusion

Friction was measured as a function of the lattice misfit of the contacting surfaces by using UHV-STM and found that the experimental results agreed with theoretical predictions. Friction was not observed when the surfaces contact with lattice misfit along sliding direction in measurements capable of resolving a friction force of 3×10^{-9} N, whereas friction with a magnitude of 8×10^{-8} N, which is comparable to theoretical values, was observed when the surfaces contact without lattice misfit along sliding direction. It has been observed

that the friction forces in some single crystals change with the crystallographic direction of sliding, and these changes were interpreted in terms of the preferred slip system in which lattice slip is likely to occur on a primary slip plane [25, 26]. However, the changes in friction force observed here due to lattice misfit were much larger, by a factor of 15, than those observed in such single crystals. It is thus concluded that the observed dependence of friction force on the lattice misfit of the contacting surfaces agrees with the theoretical predictions, which will be described in next Chapter.

Chapter 4

Atomistic Locking and Friction

4.1 Introduction

This chapter theoretically considers the atomistic origin of frictional force on clean solid surfaces. It clarifies the origin of the frictional force that is generated by intrinsic factors, such as molecular interactions between constituent atoms, not by extrinsic factors such as surface asperities or surface contaminants. The system studied consists of two solid crystals; the upper and lower body. The lower body is assumed to be rigid, and the upper body slides against it. The atoms belonging to both bodies are assumed to interact with each other by pairwise interatomic potentials. The frictional properties are investigated for a quasistatic case where the upper body slides very slowly against the lower one. Atoms are considered to form the most favorable configuration by changing their positions during quasistatic sliding. Thus the concept of adiabatic potential is introduced to analyze the interaction energy operating between all the constituent atoms and the changes in their configurations. In general, the configuration of the atoms changes either continuously or discontinuously during sliding. The energy necessary for these configuration of the atoms to change is the frictional energy. This energy could dissipate into lattice vibrations, but the detailed mechanisms of such energy dissipation are not investigated here.

The organization of this chapter is as follows: Section 4.2 defines the model for friction. The expressions for the adiabatic potential, frictional energy, and frictional force are obtained by assuming a rigid lower body. Section 4.3 examines an unrelaxed upper body case, in which both of the upper and lower bodies are assumed to be rigid, by allowing the interplanar distance between the two bodies to vary during sliding. In this case, the configuration of the atoms continuously changes, resulting in one atomistic origin called *atomistic locking*. Section 4.4V analyzes a relaxed upper body case, where the upper body is allowed to relax during sliding, in relation to the strength of the interaction potential existing between the two sliding bodies. In this case, the configuration of the atoms changes either continuously or discontinuously during sliding. The discontinuous change of the configuration results in the other atomistic origin called *dynamic locking*. In addition, friction transition is observed where friction force changes from vanishing to finite as the interaction potential strengthens and a criterion for this occurrence is derived. Section 4.5 discusses the frictional properties of various systems in connection with the friction

transition analyzed in section 4.4.

4.2 Theoretical preliminaries

4.2.1 Adiabatic potential

The adiabatic potential is defined by the total energy when two contacting solid bodies slide against each other. This assumes that the upper body slides against a fixed lower body. It is also assumed that the upper body has N^u atoms and the lower body N^l atoms, and that the constituent atoms belonging to both bodies interact with each other. The position coordinates of the atoms are denoted by $\vec{r}_i = (r_i^x, r_i^y, r_i^z)$ where $i = 1, 2, \ldots, (N^u + N^l)$. Total energy is a function of the position vectors $\vec{r}_i$ of all the atoms,

$$W(\vec{Q} : \{\vec{r}_i\}). \tag{4.1}$$

$\vec{Q}$ stands for the displacement vector of the upper body against the lower body. An $\vec{r}_i$ coordinate set satisfies the relationship

$$\vec{Q} = \sum_i^{N^u} \vec{r}_i / N^u \quad \text{and} \quad \vec{0} = \sum_i^{N^l} \vec{r}_i / N^l. \tag{4.2}$$

Thus, the adiabatic potential spans a $3(N^u + N^l - 1)$-dimensional potential surface. A set of $\vec{r}_i$ is determined so as to minimize $W(\vec{Q} : \{\vec{r}_i\})$ for a given $\vec{Q}$. The adiabatic potential can then be denoted as $W(\vec{Q})$, since $\vec{r}_i$ is a function of $\vec{Q}$. In general, the configuration of the atoms can change either continuously or discontinuously as $\vec{Q}$ varies.

Suppose $\vec{Q}$ and $\vec{Q}'$ are very close. Frictional energy $W(\vec{Q}, \vec{Q}')$ is defined as the energy necessary for the configuration at $\vec{Q}'$ to change into the one at $\vec{Q}$. Thus, frictional force $\vec{F}(\vec{Q})$ and critical frictional force $\vec{F}_c$, which are required to slide two contacting bodies against each other, can be obtained by

$$\vec{F}(\vec{Q}) = \lim_{\vec{Q}' \to \vec{Q}} \frac{W(\vec{Q}, \vec{Q}')}{\vec{Q} - \vec{Q}'}, \tag{4.3}$$

and

$$\vec{F}_c = \text{Maximum of } \vec{F}(\vec{Q}). \tag{4.4}$$

Frictional energy $W(\vec{Q}_1, \vec{Q}_2)$ is lost along the path from $\vec{Q}_1$ to $\vec{Q}_2$ and can be obtained by

$$W(\vec{Q}_1, \vec{Q}_2) = \int_{path} -(d\vec{Q}, \vec{F}(\vec{Q}))_i, \tag{4.5}$$

where $(\vec{x}, \vec{y})_i$ stands for an inner product between vectors $\vec{x}$ and $\vec{y}$; this notation will be used throughout this paper. Frictional energy depends on the path. Average frictional force $F_{av}(\vec{Q}_1, \vec{Q}_2)$ along a path from $\vec{Q}_1$ to $\vec{Q}_2$ is

$$F_{av}(\vec{Q}_1, \vec{Q}_2) = \frac{W(\vec{Q}_1, \vec{Q}_2)}{\int_{path} |d\vec{Q}|}. \tag{4.6}$$

Equations (4.3)-(4.6) generally hold true when any two bodies slide against each other.

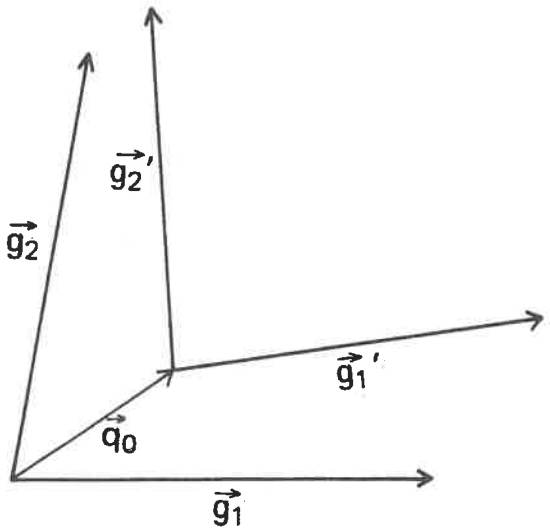

Figure 4.1: General configuration where the primitive cell is spanned by primitive vectors: $\vec{g}_1'$ and $\vec{g}_2'$ of the upper body and contacts a primitive cell spanned by primitive vectors: $\vec{g}_1$ and $\vec{g}_2$ of the lower body with misfit vector q_0.

4.2.2 Model

The model involves two contacting surfaces that have some form of simple symmetry for simplification such as fcc (face-centered cubic), bcc (body-centered cubic) or hcp (hexagonal closed packed) lattices. Each atom belonging to the upper (or lower) body is denoted by a (or b).

$$V_{aa}(r), \quad V_{ab}(r), \quad \text{and} \quad V_{bb}(r). \tag{4.7}$$

$V_{cd}(r)$ $(c, d = a \text{ or } b)$ describes the interaction between atoms c and d (r: the interatomic distance between two atoms). $V_{ab}(0) = 0$ and $V_{aa}(0) = 0$ are used throughout this paper. This assumption means the exclusion of the self-energy part of the interactions between constituent atoms from the expressions derived below. This is equivalent to $\sum'$, where the summation when $i = j$ in eq.(4.8), for example, is excluded. The relative positions for the primitive vectors of the two contact surfaces are shown in Fig. 4.1. These primitive vectors are denoted by $\vec{g}_1'$, $\vec{g}_2'$, $\vec{g}_1$, and $\vec{g}_2$ and $\vec{q}_0$ is a misfit vector. The following section studies frictional properties for when an upper body moves quasistatically along a certain direction parallel to the contacting surface against a stationary lower body.

4.2.3 Expression for adiabatic potential

The adiabatic potential is obtained by

$$W(\vec{Q}) = \sum_{i}^{N^u} \sum_{j}^{N^l} V_{ab}(|\vec{r}_i - \vec{r}_j|) + \frac{1}{2} \sum_{i,j}^{N^u,N^u} V_{aa}(|\vec{r}_i - \vec{r}_j|). \tag{4.8}$$

Remember that $V_{ab}(0) = 0$ and $V_{aa}(0) = 0$. Here, the summation of j in the first term of the right hand side is expressed by

$$V^l(r) = \sum_j^{N^l} V_{ab}(|\vec{r} - \vec{r}_j|). \tag{4.9}$$

$V^l(r)$ is the interaction energy that the atoms of the upper body receive from the atoms of the lower body. The terms $V_{bb}(|\vec{r}_i - \vec{r}_j|)$ is dropped, since it has no $\vec{Q}$-dependence. $V^l(r)$ has a periodicity characterized by the primitive vectors of the top layer of the lower body. Also, an upper body with a simple symmetry can be regarded as a stacked layered crystal. Equation (2.8) can be rewritten by making use of these facts.

A new notation $\vec{r}_i^{\gamma}$ or $(\vec{\rho}_i^{\gamma}, z_i^{\gamma})$ is introduced, where $\vec{\rho}_i^{\gamma}$ stands for the components of the positional vectors on the γth layer, which is referenced by counting γ layers up from the bottom layer of the upper body. z_i^{γ} stands for the z components of the positional vectors on the γth layer. Notation $\vec{r}_i = (r_i^x, r_i^y, r_i^z)$ is still used in section IV and positional vector $\vec{r}_i^{\gamma}$ can be expressed by using primitive vectors $\vec{g}_1$ and $\vec{g}_2$ of the lower body:

$$\vec{r}_i^{\gamma} = (\vec{\rho}_i^{\gamma}, z_i^{\gamma}) = (x_i^{\gamma}\vec{g}_1 + y_i^{\gamma}\vec{g}_2 + \Delta\vec{\rho}_i^{\gamma}, z_i^{\gamma}), \tag{4.10}$$

Here $\Delta\vec{\rho}_i^{\gamma}$ is defined by

$$\Delta\vec{\rho}_i^{\gamma} = \Delta x_i^{\gamma}\vec{g}_1 + \Delta y_i^{\gamma}\vec{g}_2, \quad (0 \le \Delta x_i^{\gamma}, \Delta y_i^{\gamma} < 1). \tag{4.11}$$

x_i^{γ} and y_i^{γ} are integers that define $\Delta\vec{\rho}_i^{\gamma}$ in eq. (4.11). x_i^{γ}, y_i^{γ}, Δx_i^{γ}, and Δy_i^{γ} are obtained from a given vector $\vec{\rho}_i^{\gamma}$ as

$$x_i^{\gamma} = [X_i^{\gamma}] \quad \text{and} \quad y_i^{\gamma} = [Y_i^{\gamma}], \tag{4.12}$$

and

$$\Delta x_i^{\gamma} = X_i^{\gamma} - [X_i^{\gamma}] \quad \text{and} \quad \Delta y_i^{\gamma} = Y_i^{\gamma} - [Y_i^{\gamma}]. \tag{4.13}$$

X_i^{γ} and Y_i^{γ} are defined by

$$X_i^{\gamma} = \frac{(\vec{\rho}_i^{\gamma}, \vec{g}_1)_i}{|\vec{g}_1|} \quad \text{and} \quad Y_i^{\gamma} = \frac{(\vec{\rho}_i^{\gamma}, \vec{g}_2)_i}{|\vec{g}_2|}. \tag{4.14}$$

where $[x]$ is Gauss's notation and stands for a maximum integer that is equal to or smaller than x. Accordingly, equation (4.8) is rewritten as,

$$W(\vec{Q}) = \begin{cases} \int d\vec{r} P(\vec{r}; \vec{g}_1, \vec{g}_2) V^l(r) + \frac{1}{2}\sum_{i,j,\gamma,\gamma'}^{N^u,N^u} V_{aa}(|\vec{r}_i^{\gamma} - \vec{r}_j^{\gamma'}|), \\ \text{or} \\ \sum_{\gamma} \int d\vec{r} P_{\gamma}(\vec{r}; \vec{g}_1, \vec{g}_2) \times [V^l(r) + \frac{1}{2}\sum_{j,\gamma'}^{N^l} V_{aa}(|\vec{r} - \vec{r}_j^{\gamma'}|)], \end{cases} \tag{4.15}$$

$$P(\vec{r}; \vec{g}_1, \vec{g}_2) = \sum_{\gamma} P_{\gamma}(\vec{r}; \vec{g}_1, \vec{g}_2), \tag{4.16}$$

$$P_{\gamma}(\vec{r}; \vec{g}_1, \vec{g}_2) = \sum_i \delta(\vec{\rho} - \Delta\vec{\rho}_i^{\gamma}) \times \delta(z - z_i^{\gamma}). \tag{4.17}$$

where $\delta(z)$ is a Delta function.

Frictional properties are studied for two cases; a rigid upper body and a relaxed upper body. In the first case, the frictional properties can be easily analyzed, and the first important result of this paper is based on this analysis. In the second, the configuration of the atoms changes either continuously or discontinuously according to displacement $\vec{Q}$.

4.3 The case of unrelaxed upper body

4.3.1 Adiabatic potential

It is assumed that the atoms of the upper body do not change their position coordinates due to sliding friction and that the configuration of the atoms of the upper body does not change with $\vec{Q}$. Therefore, the first term in the right hand side of eq. (4.15) is focused on, since only $\vec{Q}$-dependence of $W(\vec{Q})$ is of interest. The equations to be solved are

$$W(\vec{Q}) = \sum_{\gamma} \int d\vec{r} P_{\gamma}(\vec{r}; \vec{g}_1, \vec{g}_2) V^{l}(r), \tag{4.18}$$

$$P_{\gamma}(\vec{r}; \vec{g}_1, \vec{g}_2) = \delta(z - h_{\gamma}) \bar{P}_{\gamma}(\vec{\rho}), \tag{4.19}$$

$$\bar{P}_{\gamma}(\vec{\rho}) = \sum_{i} \delta(\vec{\rho} - \Delta\vec{\rho}_i^{\gamma}), \tag{4.20}$$

$$\Delta\vec{\rho}_i^{\gamma} = \Delta x_i^{\gamma} \vec{g}_1 + \Delta y_i^{\gamma} \vec{g}_2. \tag{4.21}$$

where $z_i^{\gamma} = h_{\gamma}$ can designate all atoms belonging to the γth layer of the upper body, since the upper body is rigid. Equation (4.17) is then rewritten as eq.(4.19) and h_{γ} is determined so as to minimize the $W(\vec{Q})$ for a given $\vec{Q}$.

The frictional properties appear as the $\vec{Q}$-dependence of $\bar{P}_{\gamma}(\vec{\rho})$ throughout eqs. (3.1)–(3.4). If, for example, $\bar{P}_{\gamma}(\vec{\rho})$ is independent on $\vec{Q}$, a given set of h_{γ} is also independent on $\vec{Q}$, since the functional form of $W(\vec{Q})$ for h_{γ} does not change. Accordingly, $\bar{P}_{\gamma}(\vec{\rho})$ and $W(\vec{Q})$ are invariant for any displacement $\vec{Q}$ and the corresponding frictional force exactly vanishes. If $\bar{P}_{\gamma}(\vec{\rho})$ changes with $\vec{Q}$, then $W(\vec{Q})$ depends on $\vec{Q}$, and the frictional force does not vanish. Thus, the $\vec{Q}$-dependence of $\bar{P}_{\gamma}(\vec{\rho})$ determines the $\vec{Q}$-dependence of $W(\vec{Q})$; i.e., it determines whether or not the frictional force vanishes. This property is crucial in the unrelaxed case, but not so important to the relaxed case where the configuration of the atoms can discontinuously change with $\vec{Q}$.

4.3.2 $\vec{Q}$-dependence of $\bar{P}_{\gamma}(\vec{\rho})$

This section examines the conditions that determine whether or not $\bar{P}_{\gamma}(\vec{\rho})$ is invariant for $\vec{Q}$. To calculate Δx_i^{γ} and Δy_i^{γ} in eq.(4.21), it is necessary to specify positional vector $\vec{\rho}_i^{\gamma}$. If the upper body is rigid, the positional vectors of the atoms belonging to the γth layer of the upper body (see Fig. 4.1) are

$$\vec{\rho}_i^{\gamma} = i_1'^{\gamma} \vec{g}_1' + i_2'^{\gamma} \vec{g}_2' + \vec{q}_0^{\gamma} + \vec{Q}, \tag{4.22}$$

where $\vec{q}_0^{\gamma}$ is a misfit vector of the γth layer. Then,

$$\begin{pmatrix} X_i^{\gamma} \\ Y_i^{\gamma} \end{pmatrix} = \begin{pmatrix} \frac{(\vec{\rho}_i^{\gamma}, \vec{g}_1)_i}{|\vec{g}_1|} \\ \frac{(\vec{\rho}_i^{\gamma}, \vec{g}_2)_i}{|\vec{g}_2|} \end{pmatrix} = \begin{pmatrix} \frac{i_1'^{\gamma}(\vec{g}_1', \vec{g}_1)_i + i_2'^{\gamma}(\vec{g}_2', \vec{g}_1)_i + (\vec{q}_0^{\gamma} + \vec{Q}, \vec{g}_1)_i}{|\vec{g}_1|} \\ \frac{i_1'^{\gamma}(\vec{g}_1', \vec{g}_2)_i + i_2'^{\gamma}(\vec{g}_2', \vec{g}_2)_i + (\vec{q}_0^{\gamma} + \vec{Q}, \vec{g}_2)_i}{|\vec{g}_2|} \end{pmatrix} \tag{4.23}$$

The two-dimensional distribution, $\bar{P}_\gamma(\vec{\rho})$, in eq.(3.3) can be obtained according to the Bohl-Sierpinski-Weyl equipartition theorem [57]. $\bar{P}_\gamma(\vec{\rho})$ is specifically determined by projecting Δx_i^γ and Δy_i^γ onto the two dimensional space spanned by vectors $\vec{g}_1$ and $\vec{g}_2$ due to eqs. (4.13) and (4.23). The equipartition theorem says that rational $(\vec{g}'_m, \vec{g}_n)_i/|\vec{g}_n|$ (m, n=1 or 2) results in a inhomogeneous $\bar{P}_\gamma(\vec{\rho})$, but irrational $(\vec{g}'_m, \vec{g}_n)_i/|\vec{g}_n|$ (m, n=1 or 2) results in a homogeneous $\bar{P}_\gamma(\vec{\rho})$. Thus, whether or not $(\vec{g}'_m, \vec{g}_n)_i/|\vec{g}_n|$ (m, n=1 or 2) is irrational or rational determines $\bar{P}_\gamma(\vec{\rho})$. The possible combinations of $(\vec{g}'_m, \vec{g}_n)_i/|\vec{g}_n|$ generate 9 kinds of $\bar{P}_\gamma(\vec{\rho})$, which are classified into three cases in terms of the $\vec{Q}$-dependence of $\bar{P}(\vec{\rho})$. The corresponding distributions for $\bar{P}(\vec{\rho})$ are schematically illustrated in Figs.2 - 4.

A. variant $\bar{P}_\gamma(\vec{\rho})$ case.

Figure 4.2 shows $\bar{P}_\gamma(\vec{\rho})$ by lines and dots. For instance, when the values for $(\vec{g}'_m, \vec{g}_n)_i/|\vec{g}_n|$ (m, n=1 or 2) are all rational, $\bar{P}_\gamma(\vec{\rho})$ consists of dots seen in Fig. 4.2(a), since many atoms can occupy the same site in a two-dimensional space. The large dots represent a relatively high density of the projected atoms. When $\vec{Q}$ varies, the dots relocate with $\vec{Q}$ and friction force appears. The occurrence of friction stems from the fact that the upper body moves against the lower body in the (non flat) potential surface. This is the same as the classical picture of friction; mechanical locking[8] of surface asperities. This potential surface, however, spans not on a large scale, but on an atomistic scale and related mechanism is called *atomistic locking*, as an analogy for the mechanism for the mechanical locking. (This situation is later referred to as the variant $P_1(\vec{r}; \vec{g}_1, \vec{g}_2)$ case.)

B. invariant $\bar{P}_\gamma(\vec{\rho})$ case.

In Fig. 4.3, $\bar{P}(\vec{\rho})$ involves only domain. The domain does not change for any direction of $\vec{Q}$. As a result, the frictional force always vanishes, since $\bar{P}(\vec{\rho})$ is invariant for any $\vec{Q}$. (This situation is referred to later as the invariant $P_1(\vec{r}; \vec{g}_1, \vec{g}_2)$ case.)

C. restricted invariant $\bar{P}_\gamma(\vec{\rho})$ case.

In Fig. 4.4, $\bar{P}(\vec{\rho})$ involves lines and domains. The domains do not change for any $\vec{Q}$. The lines, however, do relocate if $\vec{Q}$ is across the lines, but do not relocate if $\vec{Q}$ is along the lines. Thus, the friction force will only vanish for a $\vec{Q}$, which is along the lines, but otherwise appears. (This situation is referred to later as the restricted invariant $P_1(\vec{r}; \vec{g}_1, \vec{g}_2)$ case.)

4.4 A more realistic case: a relaxed upper body

Only atoms belonging to the bottom layer of the upper body can change their position coordinates when two bodies slide against each other. This assumption is plausible, since the relaxation of atoms in the other layers, such as the 2nd, 3rd, ..., would probably be small compared to those of the bottom layer. Two extreme limits for $V^l(r)$ (weak and strong) are studied to see what occurs when $V_{ab}(r)$ becomes stronger.

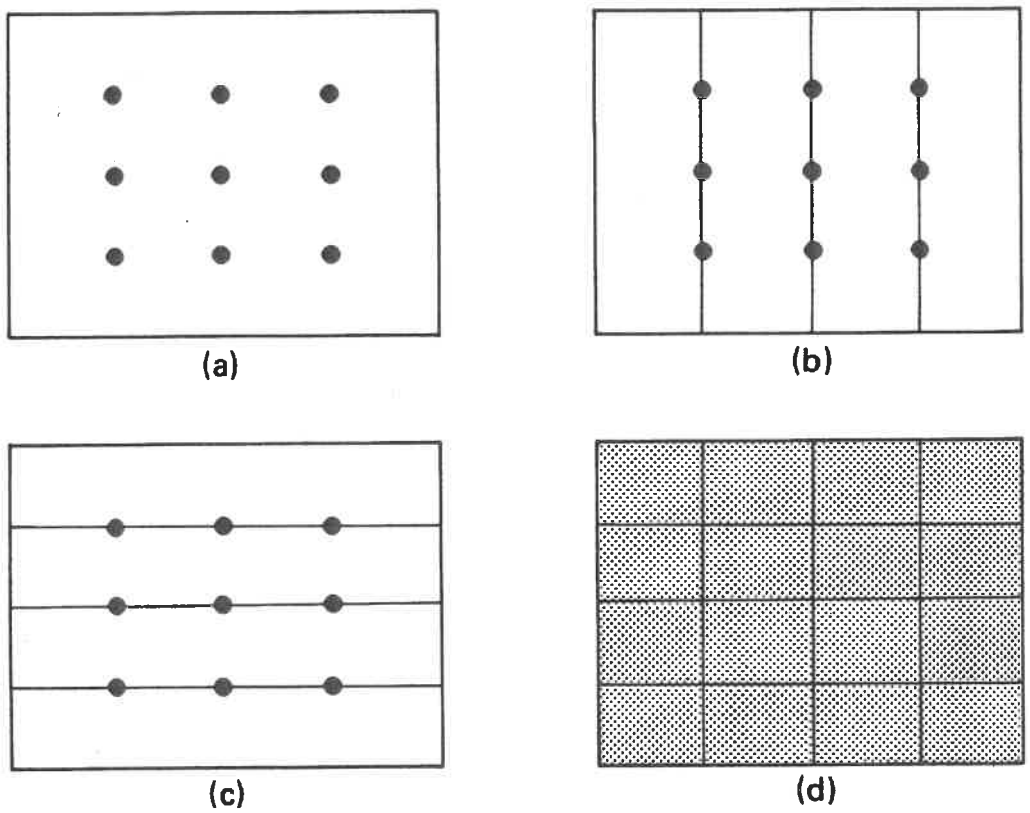

Figure 4.2: Schematic illustrations of possible non-vanishing regions where the atoms of the upper body are projected onto a two-dimensional space spanned by g_1 and g_2 when $\bar{P}_\gamma(\vec{\rho})$ is variant with $\vec{Q}$. $(\frac{(\vec{g}_1',\vec{g}_1)_i}{|\vec{g}_1|}, \frac{(\vec{g}_2',\vec{g}_1)_i}{|\vec{g}_1|}, \frac{(\vec{g}_1',\vec{g}_2)_i}{|\vec{g}_2|}, \frac{(\vec{g}_2',\vec{g}_2)_i}{|\vec{g}_2|}) = (r,r,r,r)$ for (a), (r,r,ir,r) or (r,r,r,ir) for (b), (r,ir,r,r) or (ir,r,r,r) for (c), and (r,ir,r,ir) or (ir,r,r,ir) or (r,ir,ir,r) or (ir,r,ir,r) for (d), where r represents rationality and ir irrationality.

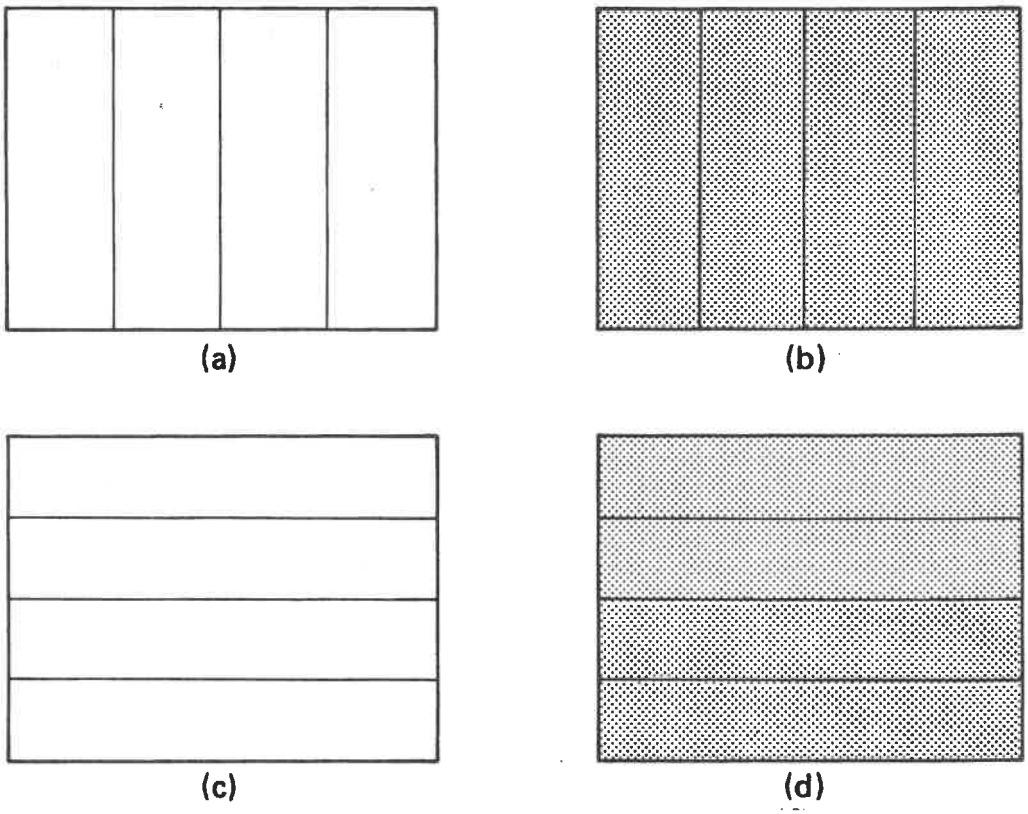

Figure 4.3: Schematic illustrations of possible non-vanishing regions where the atoms of the upper body are projected onto a two-dimensional space spanned by g_1 and g_2 when $\bar{P}_\gamma(\vec{\rho})$ is invariant with $\vec{Q}$. $(\frac{(\vec{g}_1',\vec{g}_1)_i}{|\vec{g}_1|}, \frac{(\vec{g}_2',\vec{g}_1)_i}{|\vec{g}_1|}, \frac{(\vec{g}_1',\vec{g}_2)_i}{|\vec{g}_2|}, \frac{(\vec{g}_2',\vec{g}_2)_i}{|\vec{g}_2|}) = (ir, ir, ir, ir)$, where ir represents irrationality.

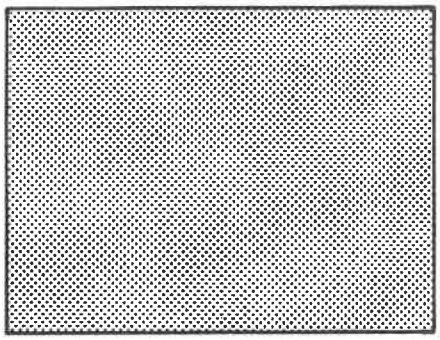

Figure 4.4: Schematic illustrations of possible non-vanishing regions where the atoms of the upper body are projected onto a two-dimensional space spanned by g_1 and g_2 when $\bar{P}_\gamma(\vec{\rho})$ invariance with $\vec{Q}$ is restricted. $(\frac{(\vec{g}_1',\vec{g}_1)_i}{|\vec{g}_1|}, \frac{(\vec{g}_2',\vec{g}_1)_i}{|\vec{g}_1|}, \frac{(\vec{g}_1',\vec{g}_2)_i}{|\vec{g}_2|}, \frac{(\vec{g}_2',\vec{g}_2)_i}{|\vec{g}_2|}) = (r, r, ir, ir)$ for (a), (r, ir, ir, ir) or (ir, r, ir, ir) for (b), (ir, ir, r, r) for (c), and (ir, ir, ir, r) or (ir, ir, r, ir) for (d), where r represents rationality and ir irrationality.

4.4.1 Weak limit

The three-dimensional distribution, $P_1(\vec{r}; \vec{g}_1, \vec{g}_2)$, in eq. (4.17) is studied instead of $\bar{P}_\gamma(\vec{\rho})$ in eq. (4.20). The adiabatic potential consists of the following three interactions; $V^l(r)$, $V^u(r)$ and U, which the atoms in the bottom layer receive. $V^l(r)$ is interaction from the atoms of the lower body. $V^u(r)$ is interaction from the atoms of the 2nd, 3rd, ... layers of the upper body. U is the mutual interaction that occurs between atoms belonging to the bottom layer of the upper body;

$$W(\vec{Q}) = \sum_i V^l(r_i^1) + \sum_i V^u(r_i^1) + U, \tag{4.24}$$

where

$$V^l(r) = \sum_j^{N^l} V_{ab}(|\vec{r} - \vec{r}_j|), \tag{4.25}$$

$$V^u(r) = \sum_{j,\gamma\neq 1} V_{aa}(|\vec{r} - \vec{r}_j^{\gamma}|), \tag{4.26}$$

$$U = \frac{1}{2}\sum_{i,j} V_{aa}(|\vec{r}_i^1 - \vec{r}_j^1|). \tag{4.27}$$

Since $V_{ab}(r)$, i.e., $V^l(r)$ is weak, $r_i^{1,\alpha}$ ($\alpha = x, y,$ or z) is expected to be very close to the position coordinate obtained by assuming a rigid upper body. Putting $r_i^{1,\alpha} = r_{i,0}^{1,\alpha} + \Delta r_i^\alpha$ (or $\vec{r}_i^1 = \vec{r}_{i,0}^1 + \Delta\vec{r}_i$) into eqs. (4.2)-(4.4), and then expanding by a small Δr_i^α (or $\Delta\vec{r}_i$), we have

$$\sum_i V^l(r_i) = \sum_i V^l(r_{i,0}) + \sum_{i,\alpha} \frac{\partial V^l(r_{i,0}^1)}{\partial r_{i,0}^{1,\alpha}} \times \Delta r_i^\alpha + \frac{1}{2}\sum_{i,\alpha,\beta} V_{i,i}^{l,\alpha,\beta} \times \Delta r_i^\alpha \Delta r_i^\beta, \tag{4.28}$$

$$\sum_i V^u(r_i) = \sum_i V^u(r_{i,0}) + \sum_{i,\alpha} \frac{\partial V^u(r^1_{i,0})}{\partial r^{1,\alpha}_{i,0}} \times \Delta r^\alpha_i + \frac{1}{2} \sum_{i,\alpha,\beta} V^{u,\alpha,\beta}_{i,i} \times \Delta r^\alpha_i \Delta r^\beta_i, \tag{4.29}$$

$$U = \sum_{i,j} V_{aa}(|\vec{r}^1_{i,0} - \vec{r}^1_{j,0}|) + \frac{1}{2} \sum_{i,j,\alpha,\beta} U^{\alpha,\beta}_{i,j} \times \Delta r^\alpha_i \Delta r^\beta_j, \tag{4.30}$$

where

$$V^{l,\alpha,\beta}_{i,i} = \frac{\partial^2 V^l(r_{i,0})}{\partial r^{1,\alpha}_{i,0} \partial r^{1,\beta}_{i,0}}, \tag{4.31}$$

$$V^{u,\alpha,\beta}_{i,i} = \frac{\partial^2 V^u(r_{i,0})}{\partial r^{1,\alpha}_{i,0} \partial r^{1,\beta}_{i,0}}, \tag{4.32}$$

$$U^{\alpha,\beta}_{i,j} = \begin{cases} \frac{\partial^2 V_{aa}(r^1_{ij,0})}{\partial r^{1,\alpha}_{ij,0} \partial r^{1,\beta}_{ij,0}} & \text{for } i \neq j, \\ \sum_j \frac{\partial^2 V_{aa}(r^1_{ij,0})}{\partial r^{1,\alpha}_{ij,0} \partial r^{1,\beta}_{ij,0}} & \text{for } i = j, \end{cases} \tag{4.33}$$

where $r^{1,\alpha}_{ij,0} = r^{1,\alpha}_{i,0} - r^{1,\alpha}_{j,0}$. $U^{\alpha,\beta}_{i,j}$ satisfies the relationship $U^{\alpha,\beta}_{i,i} + \sum_{j(\neq i)} U^{\alpha,\beta}_{i,j} = 0$ for $\alpha, \beta = x, y,$ or z. This is equivalent to a condition where interaction U has translational invariance, that is, U is invariant for the uniform displacements $\vec{r}_i \rightarrow \vec{r}_i + \vec{a}$ ($\vec{a}$: arbitrary constant displacement vector) of all the atoms.

When one chooses $r_{i,0}$ so as to minimize $\sum_i V^u(r_i) + U$, the adiabatic potential can be obtained by minimizing

$$\begin{aligned} W(\vec{Q} : \{\Delta r^\alpha_i\}) = & \sum_i V^l(r^1_{i,0}) + \sum_i V^u(r^1_{i,0}) + \sum_{i,j} V_{aa}(|\vec{r}^1_{i,0} - \vec{r}^1_{j,0}|) \\ & + \sum_{i,\alpha} \frac{\partial V^l(r^1_{i,0})}{\partial r^{1,\alpha}_{i,0}} \times \Delta r^\alpha_i \\ & + \frac{1}{2} \sum_{i,\alpha,\beta} [\epsilon_{i,j} \{V^{l,\alpha,\beta}_{i,j} + V^{u,\alpha,\beta}_{i,j}\} + U^{\alpha,\beta}_{i,j}] \times \Delta r^\alpha_i \Delta r^\beta_j. \end{aligned} \tag{4.34}$$

with respect to Δr^α_i, where $\epsilon_{i,j} = 1$ for $i = j$ and $\epsilon_{i,j} = 0$ otherwise. The atoms in the bottom layer feel a stronger potential from the atoms in the upper layers (2nd, 3rd, ...) than from those in the same bottom layer for a first approximation. The interaction from the bottom layer is actually 1/10 to 1/2 that from the upper layers of the fcc and bcc lattices. Mutual interaction term $U^{\alpha,\beta}_{i,j}$ is neglected for the first approximation. The derivation of the position coordinates for the atoms of the upper body can be obtained from Appendix by taking $U^{\alpha,\beta}_{i,j}$ into account. Then it is set that $V^{u,x,x}_{i,i} = \omega_x > 0$, $V^{u,y,y}_{i,i} = \omega_y > 0$, $V^{u,z,z}_{i,i} = \omega_z > 0$ and $U^{\alpha,\beta}_{i,j} = 0$ in eq. (4.34) for surfaces such as the (001) planes of the bcc lattices which have a square symmetry. For other crystal planes, the results are slightly modified. Displacement Δr^α_i, as obtained from eq. (4.34), is

$$\Delta r^\alpha_i \simeq -\frac{\partial V^l(r_{i,0})/\partial r^\alpha_{i,0}}{V^{u,\alpha,\alpha}_{i,i}} = -\frac{\partial V^l(r_{i,0})/\partial r^\alpha_{i,0}}{\omega_\alpha}. \tag{4.35}$$

This expression tells us that Δr_i^α continuously changes if $\partial V^l(r_i^\alpha)/\partial r_i^\alpha$ is a continuous function of r_i^α. In the case of a rigid upper body, $P_1(\vec{r};\vec{g}_1,\vec{g}_2)$ is obtained as $P_1(\vec{r};\vec{g}_1,\vec{g}_2) = \delta(z-h_1)\times\sum_i \delta(\vec{\rho}-\Delta\vec{\rho}_i^1) = \delta(z-h_1)\times\bar{P}_1(\vec{\rho})$. Where $P_1(\vec{r};\vec{g}_1,\vec{g}_2)$ consists of non-vanishing regions that involve the lines, dots, or domains shown in Figs.2–4. For the weak $V^l(r)$, each point in the regions slightly shifts in accordance with eq. (4.35), even though the lines, dots, or domains do not change their topology when shifts occur due to a weak $V^l(r)$. Thus, the frictional properties for a weak $V^l(r)$ are essentially the same as those in the rigid upper body case, provided the first derivative of $V^l(r)$ is a continuous function of r.

As seen in eq. (4.35), the density of $P_1(\vec{r};\vec{g}_1,\vec{g}_2)$ generally decreases as one approaches the ridge lines of $V^l(r)$. The direction along the ridge line is defined as $\partial V^l(r)/\partial r = 0$ and $\partial^2 V^l(r)/\partial r^2 < 0$ as the direction perpendicular to it. These ridge lines play a crucial role in deciding whether or not the frictional force vanishes and they will be discussed later.

4.4.2 Strong limit

Atoms in the bottom layer of the upper body position themselves at the lowest minima of potential $V^l(r)$ that is the nearest to each atom. These lowest minima positions are denoted by vectors $i_1\vec{g}_1 + i_2\vec{g}_2 + \vec{\tau}_m$ (i_1, i_2=any integer), where m denotes only one minimum when there are several lowest minima in the primitive cell of the lower body. For the (001) planes of simple crystals, such as bcc lattices, $m = 1$. Integers i_1 and i_2 in $i_1\vec{g}_1 + i_2\vec{g}_2 + \vec{\tau}_m$ nearest to $\vec{\rho}_i = i_1'\vec{g}_1' + i_2'\vec{g}_2' + \vec{q}_0 + \vec{Q}$ are determined so as to minimize the distance

$$d_{i_1,i_2} = |\{i_1\vec{g}_1 + i_2\vec{g}_2 + \vec{\tau}_m\} - \{\vec{\rho}_i = i_1'\vec{g}_1' + i_2'\vec{g}_2' + \vec{q}_0 + \vec{Q}\}| \quad \text{for a certain } m. \tag{4.13}$$

$P_1(\vec{r};\vec{g}_1,\vec{g}_2)$ is invariant for any $\vec{Q}$, since the atoms definitely occupy the positions of the lowest minima of $V^l(r)$.

Let us consider the frictional system shown in Fig. 4.5. A small displacement of $\vec{Q}$ changes a few i_1 (or i_2) into $i_1 \pm 1$ (or $i_2 \pm 1$). A few corresponding atoms then jump from site $i_1\vec{g}_1 + i_2\vec{g}_2 + \vec{\tau}_m$ to the nearest neighboring site. Frictional energy is necessary for the atoms to change beyond the potential barrier between site $i_1\vec{g}_1 + i_2\vec{g}_2 + \vec{\tau}_m$ and its nearest neighboring site. Frictional force then appears, identifying another origin of friction. The atoms discontinuously change. The appearance of the discontinuity is ascribed to the failure of the adiabatic potential description. This origin, therefore, cannot be described within the framework of the adiabatic potential. The origin can be described only by taking the dynamic movements of the atoms into account. Accordingly, this origin of friction force is referred to as *dynamic locking*. $P_1(\vec{r};\vec{g}_1,\vec{g}_2)$ is still invariant in this displacement. Dynamic locking occurs for an any arbitrarily small displacement $\vec{Q}$. friction force is, therefore, a complicated function of $\vec{Q}$.

In the variant $P_1(\vec{r};\vec{g}_1,\vec{g}_2)$ case, dynamic locking occurs infrequently. When a certain $\vec{Q}$ is given, many of the atoms throughout the entire system cooperatively jump beyond the potential barrier, since $(\vec{g}_m', \vec{g}_n)_i/|\vec{g}_n|$ (m, n=1 or 2) is rational. In the restricted invariant $P_1(\vec{r};\vec{g}_1,\vec{g}_2)$ case, dynamic locking frequently occurs only in a direction along the lines in $P_1(\vec{r};\vec{g}_1,\vec{g}_2)$.

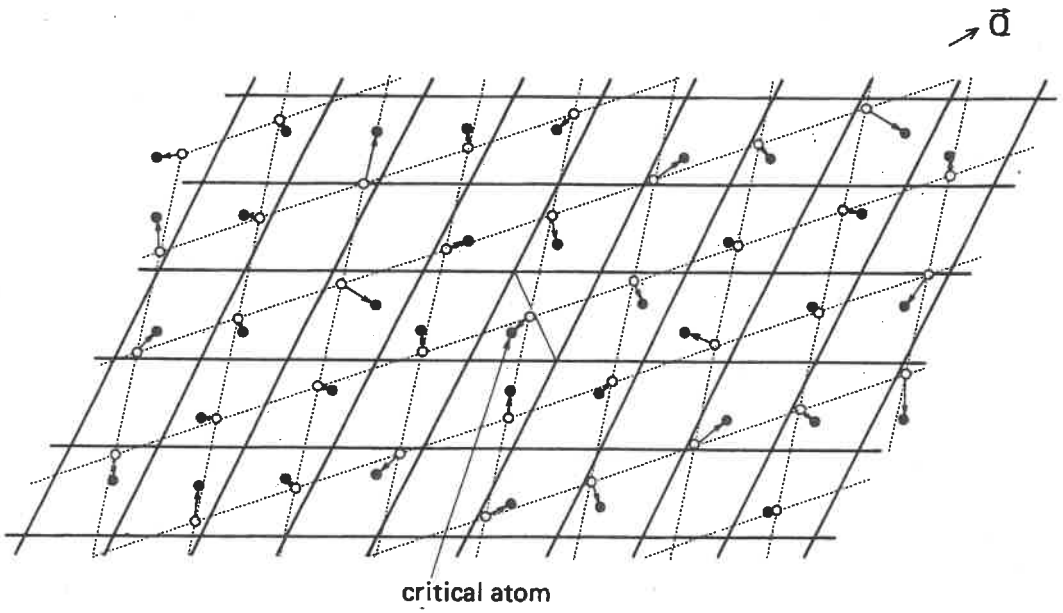

Figure 4.5: Two contacting surfaces where $P_1(\vec{r}; \vec{g}_1, \vec{g}_2)$ of the frictional system is invariant for any $\vec{Q}$. The upper body surface, shown by broken lines, contacts the lower body surface, shown by solid lines. Atoms initially positioned at symbols (o) move symbols (•), which correspond to the lowest minimum of $V^l(r)$. The critical atom near the boundary line of a primitive cell of the lower body is the one most likely to jump beyond the potential barrier when $\vec{Q}$ is given.

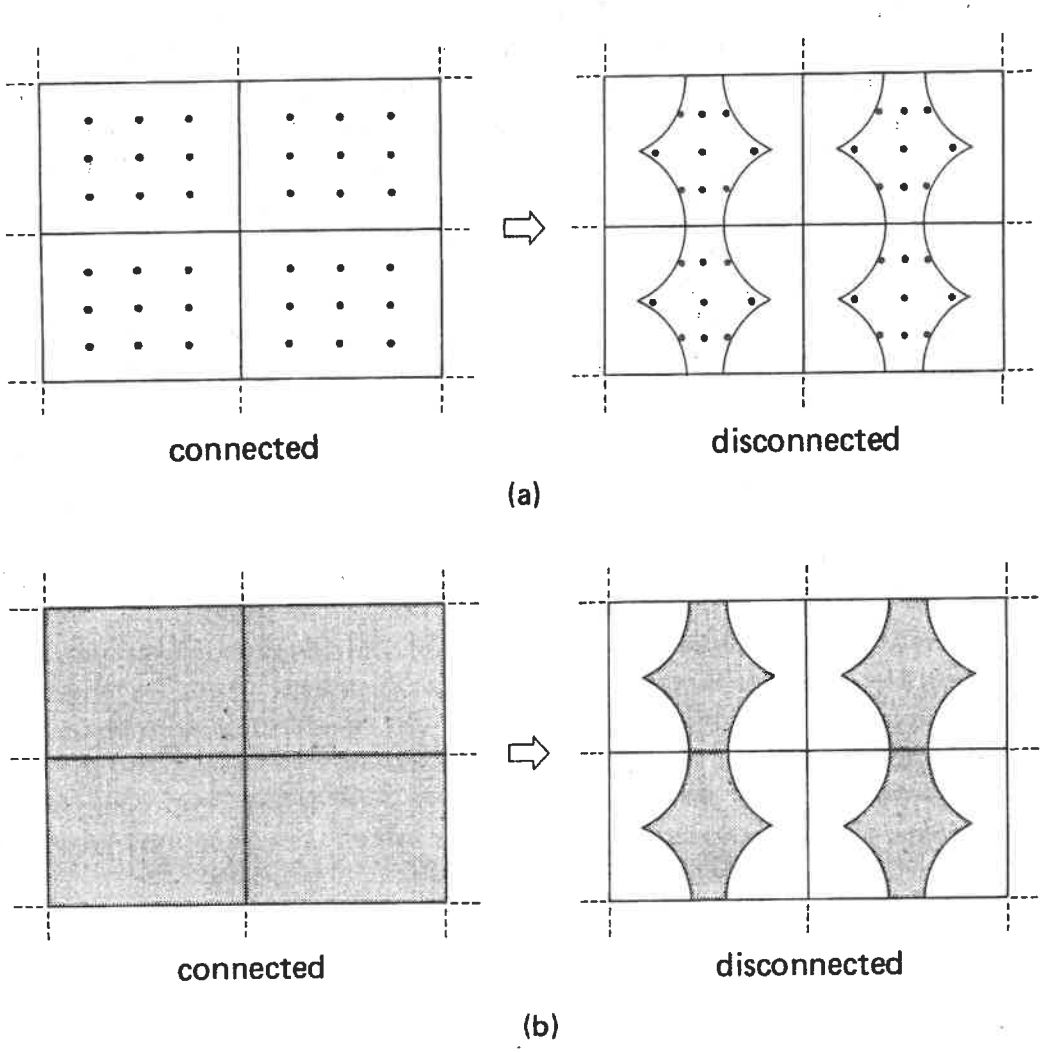

Figure 4.6: Disconnectedness of a pattern made by tiling $P_1(\vec{r};\vec{g}_1,\vec{g}_2)$ periodically. (a) is the variant $P_1(\vec{r};\vec{g}_1,\vec{g}_2)$ case, and (b) is the invariant $P_1(\vec{r};\vec{g}_1,\vec{g}_2)$ case.

4.4.3 Intermediate regime: friction transition

In the variant $P_1(\vec{r};\vec{g}_1,\vec{g}_2)$ case, the non-vanishing regions of $P_1(\vec{r};\vec{g}_1,\vec{g}_2)$ consist of many dots or lines (see Fig. 4.2) for an arbitrary strength of $V^l(r)$. $P_1(\vec{r};\vec{g}_1,\vec{g}_2)$ varies for any $\vec{Q}$ and any $V^l(r)$. When $\vec{Q}$ varies, the atoms in the upper body continuously change their positions. This leads to atomistic locking, resulting in non-vanishing friction force. The corresponding adiabatic potential and friction force is calculated by specifying the functional form of interaction $V_{ab}(r)$. As $V^l(r)$ becomes stronger, the vanishing region (where atoms can not stay) broadens in $P_1(\vec{r};\vec{g}_1,\vec{g}_2)$ for any $\vec{Q}$. Further increases in $V^l(r)$ disconnect the pattern where $P_1(\vec{r};\vec{g}_1,\vec{g}_2)$ is tiled periodically, as shown in Fig. 4.6(a), depending on the direction of $\vec{Q}$. When $\vec{Q}$ in the disconnected direction is given, the atoms only move by non-adiabatic jumping over the vanishing regions in $P_1(\vec{r};\vec{g}_1,\vec{g}_2)$. This leads to dynamic locking.

In the invariant $P_1(\vec{r};\vec{g}_1,\vec{g}_2)$ case, the non-vanishing region in $P_1(\vec{r};\vec{g}_1,\vec{g}_2)$ consists of

only the domain (see Fig. 4.3) for a weak $V^l(r)$. $P_1(\vec{r};\vec{g}_1,\vec{g}_2)$ is invariant for any $\vec{Q}$ and for a small $V^l(r)$, resulting in vanishing frictional force. Atomistic locking never occurs under these circumstances. As $V^l(r)$ becomes stronger, the vanishing region appears in $P_1(\vec{r};\vec{g}_1,\vec{g}_2)$. Further increases in $V^l(r)$ eventually disconnect the pattern where $P_1(\vec{r};\vec{g}_1,\vec{g}_2)$ is periodically tiled, shown in Fig. 4.6(b), depending on the direction of $\vec{Q}$. This results in dynamic locking due to a strong $V^l(r)$ interaction. It can thus be concluded that the transition where frictional force changes from vanishing to finite occurs due to an increased $V^l(r)$. This transition is called *friction transition.*

In the restricted invariant $P_1(\vec{r};\vec{g}_1,\vec{g}_2)$ case, the non-vanishing regions consist of lines and dots (see Fig. 4.4) if $V^l(r)$ is weak. $P_1(\vec{r};\vec{g}_1,\vec{g}_2)$ is invariant for a $\vec{Q}$ along the lines in $P_1(\vec{r};\vec{g}_1,\vec{g}_2)$ and for a weak $V^l(r)$, which results in the occurrence of vanishing frictional force only along those lines. Increases in $V^l(r)$ will cause the pattern for $P_1(\vec{r};\vec{g}_1,\vec{g}_2)$ to disconnect, depending on the direction of $\vec{Q}$. After this disconnectedness, dynamic locking occurs.

There are two atomistic origins for solid sliding friction; atomistic locking and dynamic locking. One locking concept stems from the fact that all the atoms of a contact surface will cooperatively move as seen in the variant and the restricted invariant $P_1(\vec{r};\vec{g}_1,\vec{g}_2)$ cases. The other stems from the fact that atoms independently jump beyond the nearest neighboring potential barrier due to non-adiabatic effects, as seen in all cases with a strong $V^l(r)$. It was then found that both the $\vec{Q}$-dependence of $P_1(\vec{r};\vec{g}_1,\vec{g}_2)$ and the changes in the topological properties of the patterns made by $P_1(\vec{r};\vec{g}_1,\vec{g}_2)$ determine the frictional properties in both the unrelaxed and relaxed upper body cases. A summarized diagram of this is shown in Fig. 4.7 and forms the central results of this paper.

Friction transition is same as the transition of analyticity-breaking, often called Aubry transition [58]. Aubry studied the Frenkel-Kontrowa model which is an one-dimensional system to describe the movement of defects or dislocations. Analyticity-breaking corresponds to the discontinuous change of the relaxed particle positions. For restricted invariant and invariant $P_1(\vec{r};\vec{g}_1,\vec{g}_2)$, the relaxed particle positions discontinuously change as $\vec{Q}$ varies. The friction transition demonstrates the Aubry transition for the two dimensional system.

4.4.4 Friction transition: criterion for its occurrence

A condition needs to be derived to decide whether or not friction transition occurs. Three interactions are considered for this condition; $V^l(r)$, $V^u(r)$ and $U = (1/2)\sum_{i,j} V_{aa}(|\vec{r}_i^{\,a} - \vec{r}_j^{\,a}|)$. The first two can be regarded as the external local fields that act on each atom belonging to the bottom layer of the upper body. The last is the mutual interaction term for the atoms belonging to the bottom layer of the upper body. The (approximated) criterion is obtained for a case where interaction $V^l(r)$ is sufficiently strong (cf. discussion in subsection (IV.A)) and the derived criterion for a general case is shown in the Appendix.

A simple case involving a one-dimensional system is first studied, in which only $V^l(r)$ and $V^u(r)$ operate (see Fig. 4.8). The results of that case are extended to the two-dimensional system. When $V^l(r)$=0, the atoms occupy positions that correspond to the lowest minima of $V^u(r)$. For a weak $V^l(r)$ limit, the atoms slightly change their positions towards the minimum positions of $V^l(r)$. For a strong $V^l(r)$ limit, the atoms occupy positions that

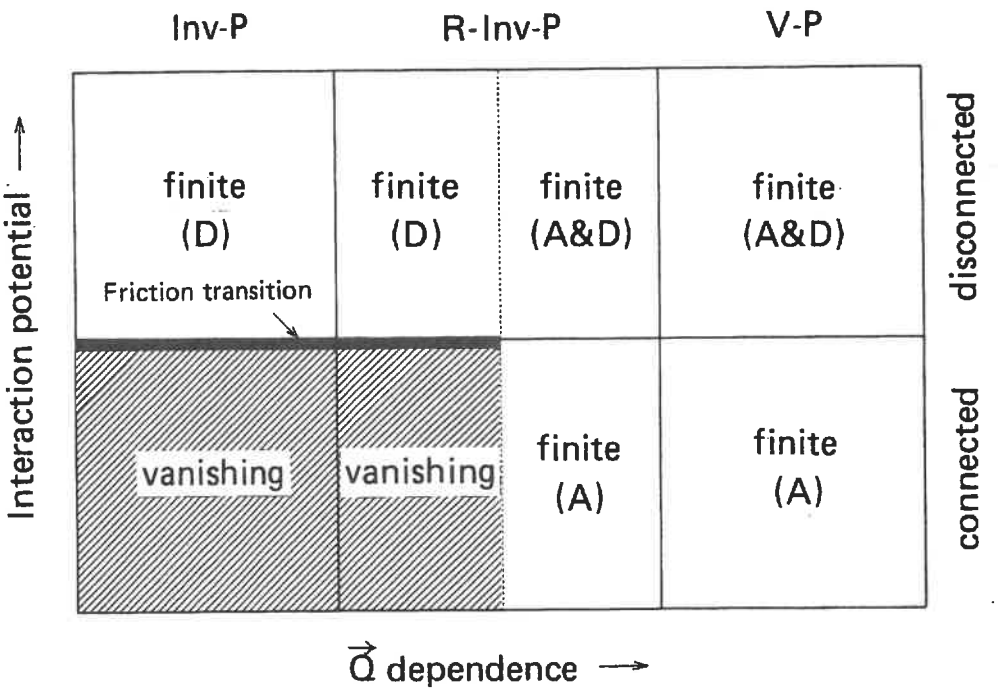

Figure 4.7: Schematic phase diagram representing whether or not friction force is finite or vanishing. Here, the invariant $P_1(\vec{r};\vec{g}_1,\vec{g}_2)$ case is denoted as Inv-P, the restricted invariant $P_1(\vec{r};\vec{g}_1,\vec{g}_2)$ case as R-Inv-P, and the variant $P_1(\vec{r};\vec{g}_1,\vec{g}_2)$ case as V-P. Atomistic locking is denoted as (A), and dynamic locking as (D).

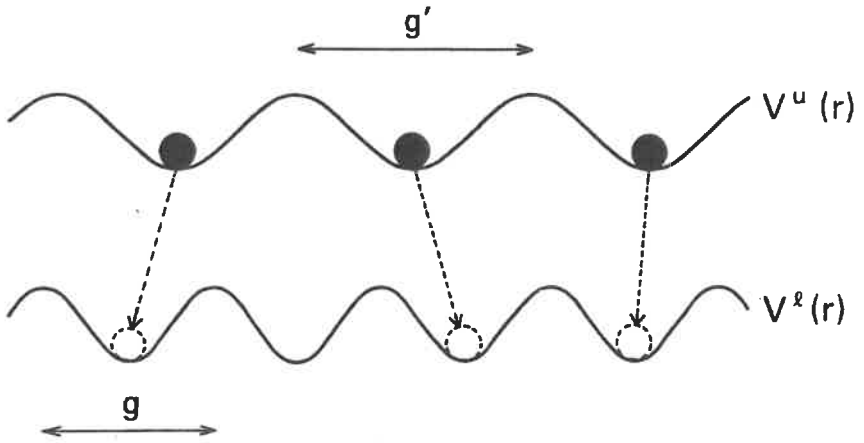

Figure 4.8: A one-dimensional frictional system. $V^l(r)$ and $V^u(r)$ have their periodicities characterized by lengths g and g'. The atoms sit on the lowest minima (•) of $V^u(r)$, when $V^l(r) = 0$. When $V^l(r)$ becomes to a strong limit, the atoms occupy the positions for the lowest minima (o) of $V^l(r)$.

correspond to the lowest minima of $V^l(r)$. When distribution $\bar{P}(r)$ is periodically arranged in a one-dimensional space, the non-vanishing regions in $\bar{P}(r)$ connect with each other for a weak $V^l(r)$, but disconnect for a strong $V^l(r)$. The friction transition that then occurs is similar to the two-dimensional case just previously mentioned and a criterion for it can be derived.

The potential energy is $V^l(r) + V^u(r)$, when r is close to the position of the extreme maxima of $V^l(r)$ and to that of the lowest minima of $V^u(r)$. If $r = r_{max} + \Delta r$ and $r = r_{min} + \Delta r'$, and $V^l(r) + V^u(r)$ is expanded by a small Δr and $\Delta r'$, then $V^l(r) + V^u(r) = V^l(r_{max}) + V^u(r_{min}) + \Delta r^2 \times d^2V^l(r_{max})/dr^2_{max} + \Delta r'^2 \times d^2V^u(r_{min})/dr^2_{min}$. Atoms are unable to occupy vanishing regions in $\bar{P}(r)$. The potential is a concave function at these positions. Since Δr is a function of $\Delta r'$: $\Delta r = r_{min} - r_{max} + \Delta r'$, and the condition under which Δr or $\Delta r'$ becomes unstable is

$$\frac{d^2V^l(r_{max})}{dr^2_{max}} + \frac{d^2V^u(r_{min})}{dr^2_{min}} < 0. \tag{4.36}$$

When $d^2V^l(r_{max})/dr^2_{max} + d^2V^u(r_{min})/dr^2_{min} \geq$ (or $<$)0, friction force vanishes (or appears).

Let us extend this criterion to a two-dimensional system. First, consider the case where U=0. r_{max} of $V^l(r)$ corresponds to a point satisfying $\partial V^l(r)/\partial r = 0$ and $\partial^2 V^l(r)/\partial r^2 < 0$ along lines that are perpendicular to the ridge lines of $V^l(r)$. For basal planes such as the (001) planes of b.c.c. lattices, the ridge lines are obtained by connecting four points of a square spanned by the two primitive vectors $\vec{g}_1$ and $\vec{g}_2$. The position on the ridge lines is denoted as $\vec{r}_s$ (or (r^x_s, r^y_s)). r_{min} of $V^u(r)$ corresponds to the lowest minima of $V^u(r)$. The potential energy expanded by a small Δr^x and Δr^y, and $\Delta r'^x$ and $\Delta r'^y$ are

$$V^l(r_s) + V^u(r_{min}) + \sum_{\alpha,\beta} V^l_{\alpha,\beta}(r_s) \times \Delta r^\alpha \Delta r^\beta + \sum_{\alpha,\beta} V^u_{\alpha,\beta}(r_{min}) \times \Delta r'^\alpha \Delta r'^\beta. \tag{4.37}$$

If the relationship between $(\Delta r^x, \Delta r^y)$ and $(\Delta r'^x, \Delta r'^y)$ is given as

$$\Delta r'^{\alpha} = \sum_{\gamma} T_{\alpha,\gamma} \Delta r^{\gamma}, \tag{4.38}$$

then equation (4.37) becomes

$$V^l(r_s) + V^u(r_{min}) + \sum_{\alpha,\beta}[V^l_{\alpha,\beta}(r_s) + \sum_{\gamma,\gamma'} V^u_{\gamma,\gamma'}(r_{min}) T_{\gamma,\alpha} T_{\gamma',\beta}] \times \Delta r^{\alpha} \Delta r^{\beta}. \tag{4.39}$$

The condition that the potential energy is a concave function of r for a one-dimensional system is equivalent to the condition that the potential energy is a concave function in a direction that is perpendicular to the ridge lines for a two-dimensional system. Denoting this direction perpendicular to the ridge lines as vector $\vec{s} = (s_x, s_y)$, the corresponding condition is

$$V_{x,x} s_x^2 + 2V_{x,y} s_x s_y + V_{y,y} s_y^2 < 0, \tag{4.40}$$

where $V_{\alpha,\beta}$ is defined by

$$V_{\alpha,\beta} = V^l_{\alpha,\beta}(r_s) + \sum_{\gamma,\gamma'} V^u_{\gamma,\gamma'}(r_{min}) T_{\gamma,\alpha} T_{\gamma',\beta} + \sum_{m} U_{\alpha,\beta}(|\vec{s} - \vec{r}^{1,m}|). \tag{4.41}$$

The effects introduced by mutual interaction U are taken in account by adding the last term in the right hand side of eq. (4.41)

4.5 Frictional properties for various systems

4.5.1 Quasistatic friction of α-iron

In this section, realistic calculations are demonstrated that relate to the quasistatic sliding friction of an α-iron. The adiabatic potentials, calculated as a function of the sliding distance, give the minimum energy necessary for sliding friction to occur. Two types of frictional systems are examined, characterized by the rationality of $(\vec{g}'_m, \vec{g}_n)_i / |\vec{g}_n|$ $(m, n{=}1 \text{ or } 2)$, where $\vec{g}'_m$ and $\vec{g}_n$ are primitive vectors of the upper and lower bodies.

Case (a) The (001) plane of an α-iron (bcc lattice) is placed against another (001) plane, as shown in Fig. 4.9(a). The upper body is then slid against the lower one in direction x. The bcc lattices that have a unit vector of $\vec{T} = (a, a, a)$ (a: a lattice constant of the bcc lattice) for the upper body are placed on the same bcc lattices of the lower body. This contact generates the variant $P_1(\vec{r}; \vec{g}_1, \vec{g}_2)$ case (see Fig. 4.2(a)), since both $(\vec{g}'_1, \vec{g}_1)_i / |\vec{g}_1|$ and $(\vec{g}'_2, \vec{g}_2)_i / |\vec{g}_2|$ are rational, $(\vec{g}'_2, \vec{g}_1)_i / |\vec{g}_1| = 0$, and $(\vec{g}'_1, \vec{g}_2)_i / |\vec{g}_2| = 0$. The upper body lattice is then commensurate with the lower body lattice both in its sliding direction x and vertical direction y.

Case (b) The (110) plane of an α-iron is placed against a (001) plane, as shown in Fig. 4.9(b). The upper body is slid against the lower one in direction x. The fct (face-centered tetragonal) lattices that have a unit vector of $\vec{T} = (a, \sqrt{2}a, a)$ for the upper body are placed on the bcc lattices that have a unit vector of $\vec{T} = (a, a, a)$ for the lower body. This contact generates the restricted invariant $P_1(\vec{r}; \vec{g}_1, \vec{g}_2)$ case (see Fig. 4.4(c)), since $(\vec{g}'_1, \vec{g}_1)_i / |\vec{g}_1|$ is rational, $(\vec{g}'_2, \vec{g}_2)_i / |\vec{g}_2|$ is irrational, $(\vec{g}'_2, \vec{g}_1)_i / |\vec{g}_1| = 0$, and $(\vec{g}'_1, \vec{g}_2)_i / |\vec{g}_2| = 0$. The upper body

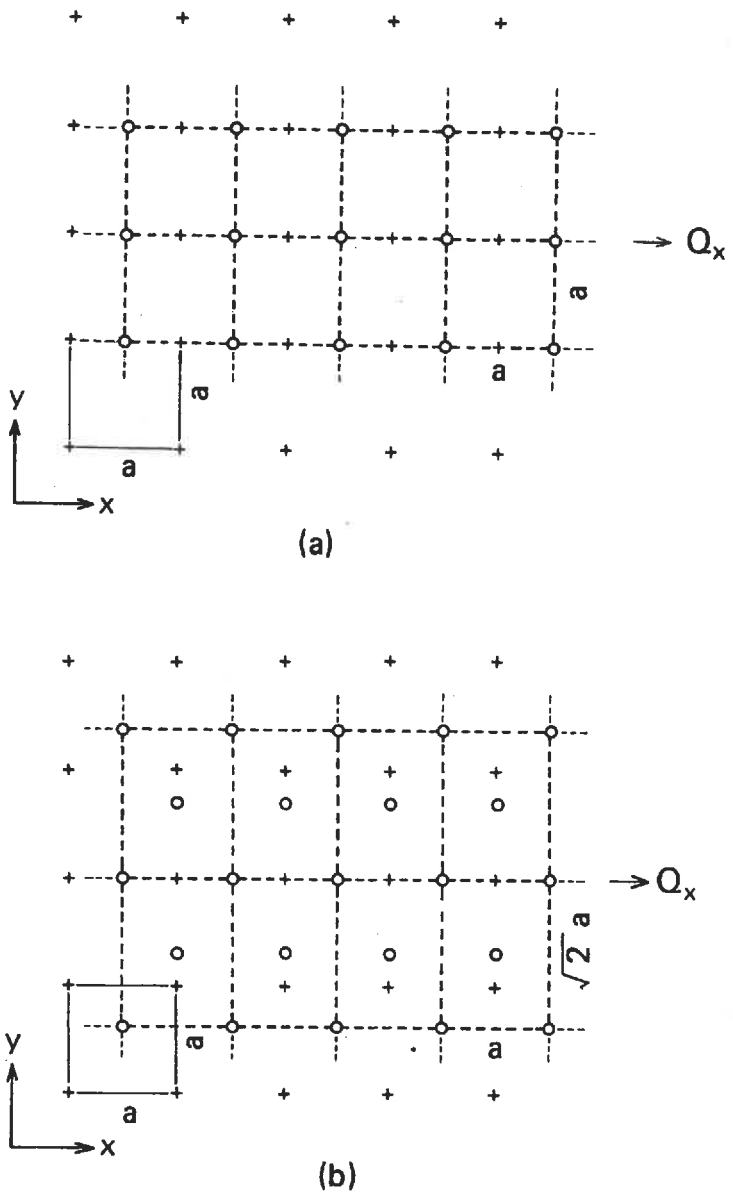

Figure 4.9: Atomic arrangements at the contact interfaces. The upper body with atoms (o) is slid over a stationary lower body with atoms (+) in the x direction. $P_1(\vec{r}; \vec{g}_1, \vec{g}_2)$ is variant with $\vec{Q}$ in any direction for (a). $P_1(\vec{r}; \vec{g}_1, \vec{g}_2)$ is invariant only with $\vec{Q}$ in the y direction for (b).

lattice is then commensurate with the lower body lattice in sliding direction x, while being incommensurate in vertical direction y.

Several kinds of interatomic potentials [59, 60, 61, 62] have been proposed for the α-iron. The Johnson potential was chosen from among them since it has been successfully used to calculate such atomic displacements as the tensile deformations of amorphous iron [63]. This potential is expressed as three third-order polynomials

$$\phi(r) = \begin{cases} -2.195976(r-3.097910)^3 + 2.704060r - 7.436448 & \text{eV} \quad \text{for } 1.9\mathring{A} < r \leq 2.4\mathring{A} \\ -0.639230(r-3.115829)^3 + 0.477871r - 1.581570 & \text{eV} \quad \text{for } 2.4\mathring{A} < r \leq 3.0\mathring{A} \\ -1.115035(r-3.066403)^3 + 0.466892r - 1.547967 & \text{eV} \quad \text{for } 3.0\mathring{A} < r \leq 3.44.\mathring{A} \end{cases} \tag{4.42}$$

The α-iron lattice constant is taken as 2.86 $\mathring{A}$. The model potential can yield reasonable surface energies for the α-iron: 1.31 J/m^2 for the (001) plane and 1.21 J/m^2 for the (110) plane. These values are comparable to a measured surface energy of 2.2 J/m^2 [64]. The frictional properties of the rigid upper body case are compared with those of the relaxed upper body case. To do this comparison, the system used is assumed to be of a sufficiently large, but finite size. The size of the adopted system is $(20 \times 20 \times 2)$ bcc unit cells (2123 atoms) for the upper body and $(24 \times 24 \times 2)$ bcc unit cells (3027 atoms) for the lower body in case (a), and $(20 \times 20 \times 2)$ fct unit cells (4203 atoms) for the upper body and $(24 \times 32 \times 2)$ bcc unit cells (4011 atoms) for the lower body in case (b).

Figure 4.10 shows adiabatic potentials normalized by contact area A as a function of sliding distance Q_x in cases (a) and (b). Potential barrier E_b can be observed in both cases. E_b changes only slightly after relaxation in case (a), but it noticeably increases after relaxation in case (b). Potential barrier E_b in case (b) is smaller than that in case (a), so less friction force appears in case (b) where $P_1(\vec{r}; \vec{g}_1, \vec{g}_2)$ is a restricted invariant. Calculation shows that E_b=1.1 J/m^2 in case (a), and E_b=0.53 J/m^2 in case (b). The average frictional forces calculated by eq. (4.6) are $F_{av}(\vec{Q}_1, \vec{Q}_2)$=7.6 GPa in case (a), and $F_{av}(\vec{Q}_1, \vec{Q}_2)$=3.7 GPa in case (b). Unfortunately, directly comparable experimental data is not available. Current experiments [13, 30] have showed highly-resolved frictional force distributions with a sensitivity ranging from 1×10^{-7} to 1×10^{-6} N by scanning very sharp 0.1 to 5 μm radius tips of diamond or Tungsten over a sputtered carbon film or a highly oriented polycrystalline graphite. The frictional forces measured are normalized by the apparent elastically contacting area and range from about 0.1 GPa to a few GPa. This suggests that the friction force resulting from atomistic locking is comparable to the friction force that will be measured in future experiments.

Another finding is that the amount of adhesion force has no relation to the friction force amount. Frictional force has often been ascribed to adhesion, i.e., chemical bonding between the actual contact surfaces in phenomenological studies [11]. In those studies, adhesion occurs at the actual contact area where the external load is concentrated. This concentrated load removes surface contaminants from the contact area, thus possibly causing the formation of adhered junctions. Accordingly, shearing force has to be applied to rupture the adhered junctions during subsequent sliding friction. friction force can, therefore, depend on shear strength and on the actual contact area where the adhered junctions are formed. When plastic deformations are introduced into the adhered junctions, the junction growth can be actually observed [12, 65]. The results, however, did not show a relationship between adhesion force and friction force.

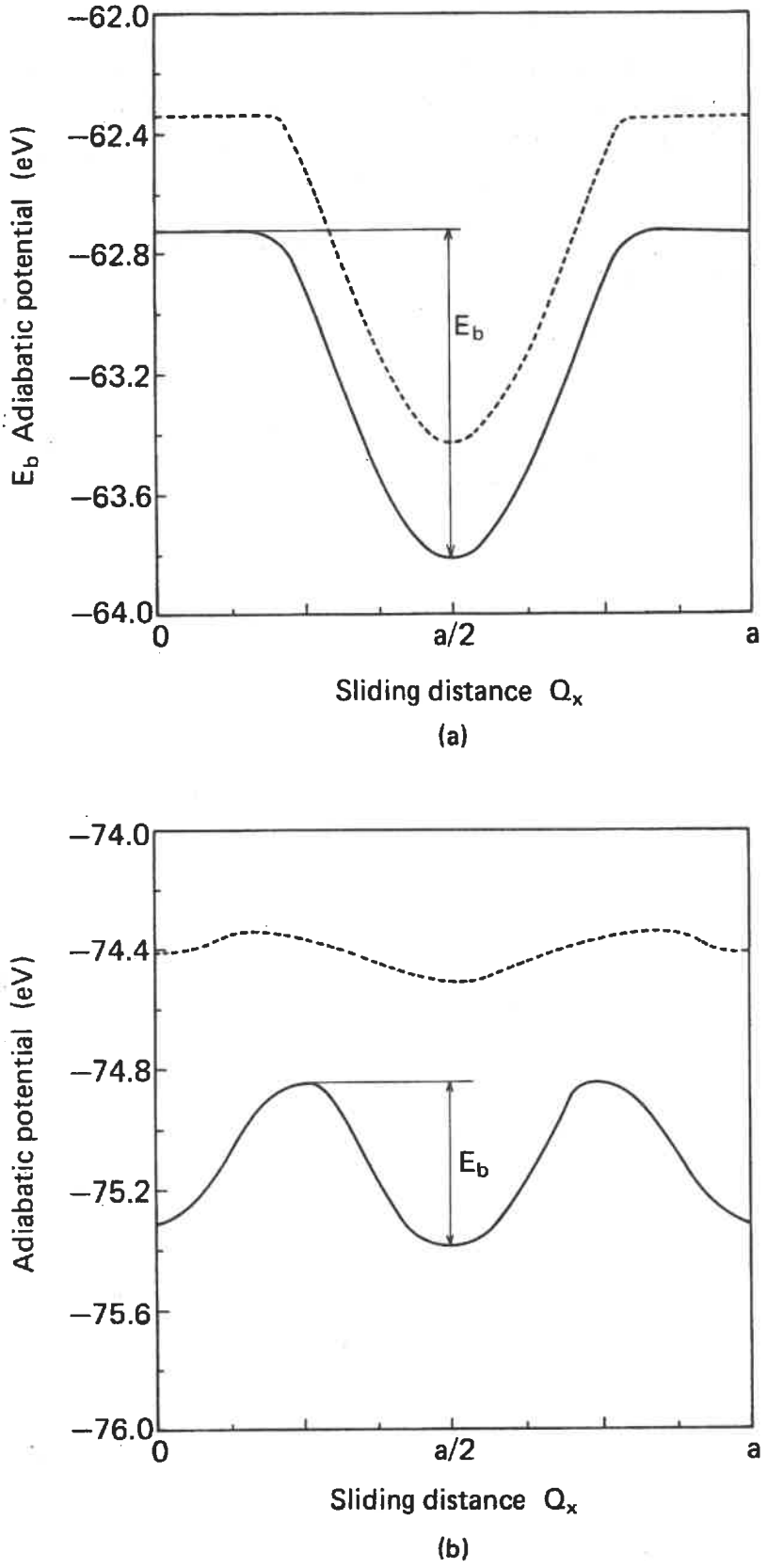

Figure 4.10: Calculated adiabatic potentials normalized by the contact area. The (001) plane of an α-iron is slid over the same (001) plane for (a), and a (110) plane over a (001) plane for (b). Broken lines represent the unrelaxed case and solid lines the relaxed one.

4.5.2 Validity of the criterion for friction transition

The criterion for friction transition states that friction transition occurs when second order derivative $V_{\alpha,\beta}$, in a direction perpendicular to a $V^l(r)$ ridge line, is negative. If distribution $P_1(\vec{r};\vec{g}_1,\vec{g}_2)$ is considered just before the friction transition occurs, the pattern is still connected by one atom (this atom is hereafter called the critical atom.) on the ridge line. The occurrence of friction transition can, therefore, be decided by judging whether or not $V_{\alpha,\beta}$ in eq. (4.41) is negative at the critical atom position.

The model verifies this consists of two contacting bodies, the (001) plane of an α-iron (upper body) that faces against the (110) plane of an α-iron (lower body) at a thirty degrees angle as shown in Fig. 4.11. The upper body is placed against the lower body so that the critical atom is positioned at the midpoint on the boundary line of the two-dimensional primitive cell of the lower body, where the critical atom feels the local minimum of the potential from the upper body, $V^u(r_{min})$, and the local maximum from the lower body, $V^l(r_{max})$. The upper body is taken to have $(20 \times 20 \times 2)$ bcc unit cells (4203 atoms) with a unit vector of $\vec{T} = (a, a, a)$, and the lower body $(24 \times 32 \times 2)$ fct unit cells (4011 atoms) with a unit vector of $\vec{T} = (\sqrt{2}a, a, \sqrt{2}a)$. At the beginning of the calculation, the rigid upper body is placed so as to minimize the total crystal energy by adjusting the interfacial separation. Next, the atoms in the upper body, excluding the critical atom, are relaxed three-dimensionally, while all of the atoms in the lower body are fixed. Two kinds of potentials are used, Morse potential and Johnson potential, as the interatomic potentials operating in the system. The Morse potential expressed as $V(r) = D(e^{-2\alpha(r-r_0)} - 2e^{-\alpha(r-r_0)})$ $(D, \alpha, r_0$: potential parameter), and is selectively applied to the atoms on the contact interface. The Johnson potential is used for the other atoms.

As seen in subsection (IV.D), the critical atom is assumed to sit on the local minimum of $V^u(r_{min})$. This assumption was confirmed by actual calculation. The calculated second-order derivatives of potential $V_{\alpha,\beta}$ in eq. (4.41) are shown as a function of Morse potential parameter D in Fig. 4.12. $V_{\alpha,\beta}$ decreases as D increases, since negative contribution $V^l(r_{max})$ from the lower body increases. The friction transition actually occurs when D is approximately 35. Figure 4.13 shows distribution $P_1(\vec{r};\vec{g}_1,\vec{g}_2)$ before relaxation and after relaxation when D=10, 20 and 60. The atoms initially move from the region around the corner of $P_1(\vec{r};\vec{g}_1,\vec{g}_2)$ (Fig. 4.13(b)), and gather toward the center of $P_1(\vec{r};\vec{g}_1,\vec{g}_2)$, where the lowest minima of potential $V^l(r)$ exists. These movements result in the cross-shaped pattern seen in Fig. 4.13(c). Just before friction transition the pattern is connected by several atoms on the boundary line in $P_1(\vec{r};\vec{g}_1,\vec{g}_2)$. After friction transition, the pattern made by $P_1(\vec{r};\vec{g}_1,\vec{g}_2)$ is completely disconnected, as shown in Fig. 4.13(d) (cf. Fig. 4.6), thus confirming the validity of the friction transition criterion.

4.5.3 Friction transition for cubic metals

The main concern here is whether or not friction transition occurs in realistic frictional systems of several fcc and bcc metals. The Morse potentials determined by Girifalco and Weitzer [62] are used as the interatomic potentials of frictional systems. The friction transition calculation follows the same procedures as in the previous section. It is assumed that only the atoms of the upper body are allowed to change their positions while the atoms of the lower body remain fixed. To satisfy this assumption the closest packed crystal

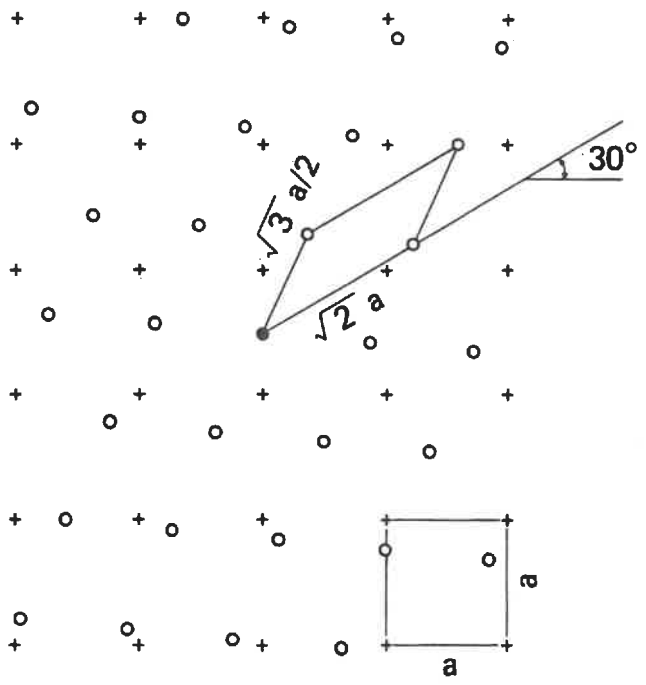

Figure 4.11: Model for friction transition. (o) symbols are upper body atoms, and (+) symbols are lower body atoms. The (•) symbol is the critical atom.

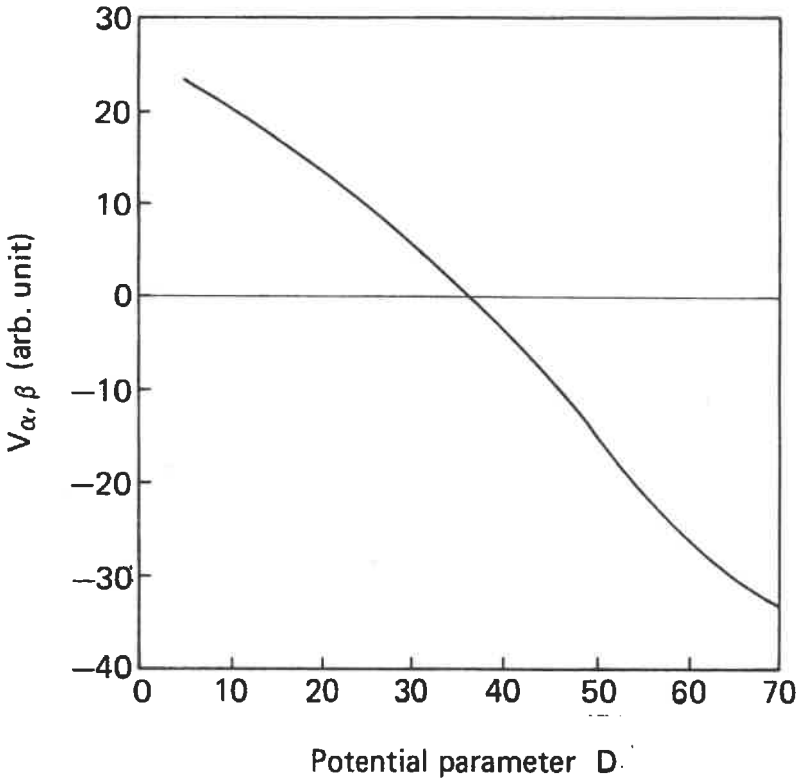

Figure 4.12: Calculated $V_{\alpha,\beta}$ as a function of Morse potential parameter D.

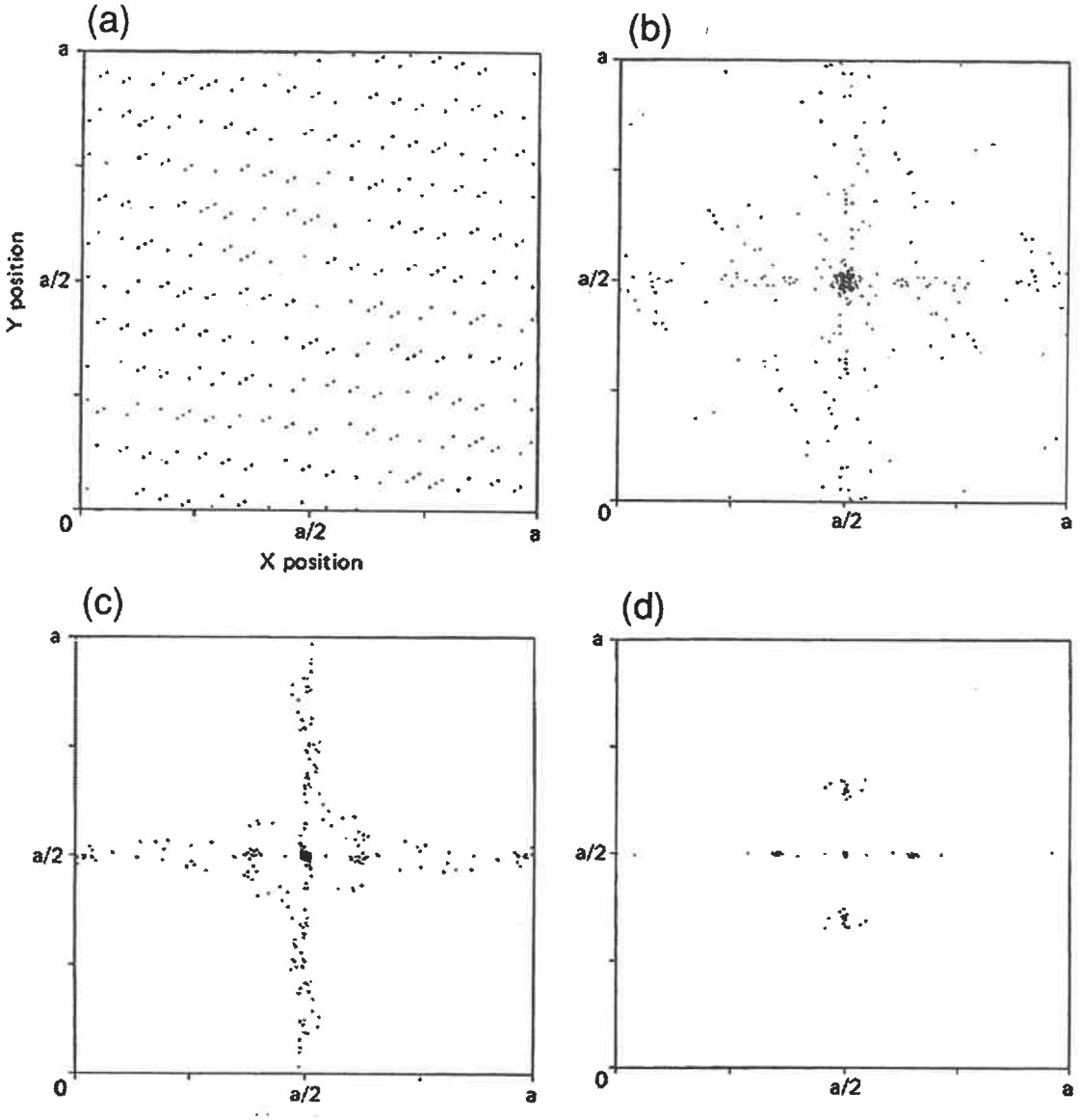

Figure 4.13: Representative distributions $P_1(\vec{r}; \vec{g}_1, \vec{g}_2)$. (a) shows distribution before relaxation. (b), (c), and (d) show distributions before relaxation when D=10, 20, and 60.

planes (hardest planes), such as the (111) planes for fcc lattices and the (110) planes for bcc lattices, are taken as the contact surfaces of the lower bodies. For fcc metals, planar atomic density increases with the (110) < (001) < (111) planes. The (110) and (001) planes are then faced against the closest packed plane (111), as shown in Figs. 4.14(a) and (b). For the (110)-(111) contact, the upper body is composed of ($18 \times 12 \times 2$) bct (body-centered tetragonal) unit cells (1173 atoms) with unit vector $\vec{T} = (a/\sqrt{2}, a, a/\sqrt{2})$ and the lower body is composed of ($29 \times 28 \times 2$) monoclinic unit cells (5858 atoms) with unit vector $\vec{T} = (a/\sqrt{2}, a/\sqrt{2}, a/\sqrt{3})$. For the (001)-(111) contact, the upper body is composed of ($11 \times 11 \times 2$) fcc unit cells (1323 atoms) with unit vector $\vec{T} = (a, a, a)$, and the lower body is composed of the same monoclinic unit cells. For bcc metals, planar atomic density increases with the (111) < (001) < (110) planes. The (001) and (111) planes are then faced against the closest packed plane (110), as shown in Figs.14(c) and (d). For the (111)-(110) contact, the upper body is composed of ($18 \times 12 \times 2$) monoclinic unit cells (1605 atoms) with unit vector $\vec{T} = (\sqrt{2}a, \sqrt{2}a, a/2\sqrt{3})$, and the lower body is composed of ($25 \times 25 \times 2$) fct unit cells (6503 atoms) with unit vector $\vec{T} = (\sqrt{2}a, a, \sqrt{2}a)$. For the (001)-(110) contact, the upper body is composed of ($18 \times 12 \times 2$) bcc unit cells (1173 atoms) with unit vector $\vec{T} = (a, a, a)$, and the lower body is composed of ($17 \times 23 \times 2$) fct unit cells (4113 atoms) with unit vector $\vec{T} = (\sqrt{2}a, a, \sqrt{2}a)$. The critical atom for each contact is placed at the point satisfying $\partial V^l(r)/\partial r = 0$ and $\partial^2 V^l(r)/\partial r^2 < 0$ along lines perpendicular to the ridge lines of $V^l(r)$, where the local minimum of potential $V^u(r_{min})$ from the upper body and the local maximum of potential $V^l(r_{max})$ from the lower body exists. In the calculation, the atoms of the upper body, excluding the critical atoms, are three-dimensionally relaxed. After relaxation second order derivative $V_{\alpha,\beta}$ is calculated for the direction perpendicular to the ridge line of each critical atom.

Figure 4.15 shows the calculated $V_{\alpha,\beta}$ as a function of Morse potential parameter D. The calculated $V_{\alpha,\beta}$ values are positive for all of the examined metals. This shows that friction transition does not occur in these frictional systems. The $V_{\alpha,\beta}$ sign is actually determined by competition between a positive $V^u(r_{min})$ contribution from the upper body and a negative $V^l(r_{max})$ contribution from the lower body as seen in eq. (4.39). A positive $V^u(r_{min})$ always defeats a negative $V^l(r_{max})$ in these frictional systems. Examining the value of $V_{\alpha,\beta}$ shows how much the frictional system is stable against friction transition. An increase in D increases the positive $V^u(r_{min})$ contribution far more than the negative $V^l(r_{min})$ contribution, thus giving a more positive $V_{\alpha,\beta}$ for the bcc metals than for the fcc ones.

It is also shown in Fig. 4.15 that $V_{\alpha,\beta}$ is dependent on the contact crystal plane. In bcc metals, for example, $V_{\alpha,\beta}$ for a (111)-(110) contact is larger than that for a (001)-(110) contact. How much $V_{\alpha,\beta}$ is dependent on the contacting crystal planes mainly depends on the differences between the positive $V^u(r_{min})$ contributions of each contact. By separating mutual contribution U (see eq. (4.27)), the atoms obtained from the bottom layer of the upper body for the total positive $V^u(r_{min})$ contribution, the partial contribution of U and its reminder in $V^u(r_{min})$ can be selectively examined. Since the (111) plane in the bcc metals has less atomic density than the (001) plane, total $V_{\alpha,\beta}$ for the (111)-(110) contact is less than for the (001)-(110) contact before relaxation. However, the final $V_{\alpha,\beta}$ for the (111)-(110) contact is inversely larger than for the (001)-(110) contact after relaxation, resulting in a large increase in the positive contributions from the upper layers (2nd, 3rd,

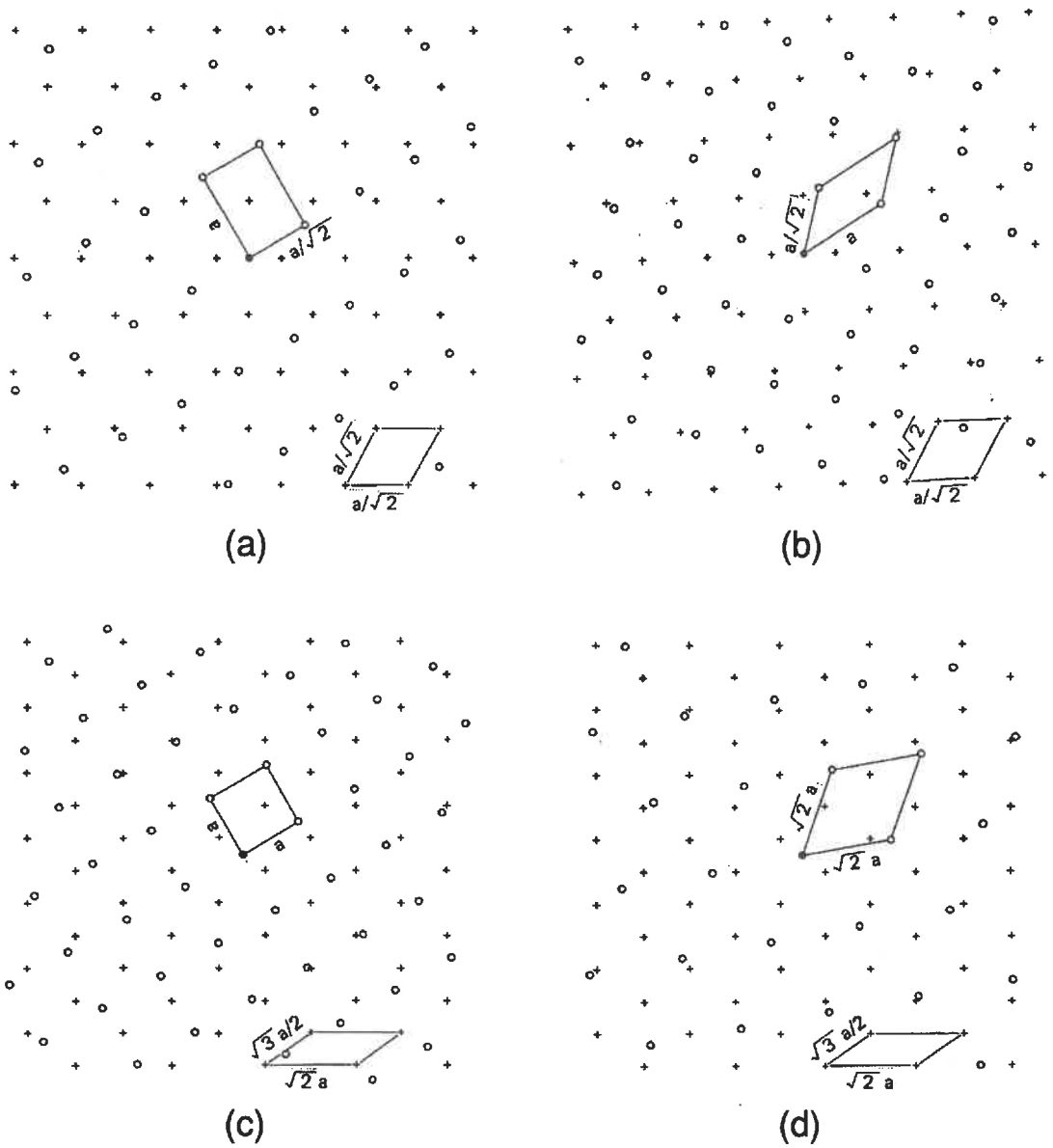

Figure 4.14: Model for friction transition in realistic systems of cubic metals. For the fcc metals, a (110)-(111) contact (a) and a (001)-(111) contact (b) are examined. For the bcc metals, a (001)-(110) contact (c) and a (111)-(110) contact (d) are examined. The (o) symbols are upper body atoms, and the (+) symbols are lower body atoms. The (•) symbol is the critical atom.

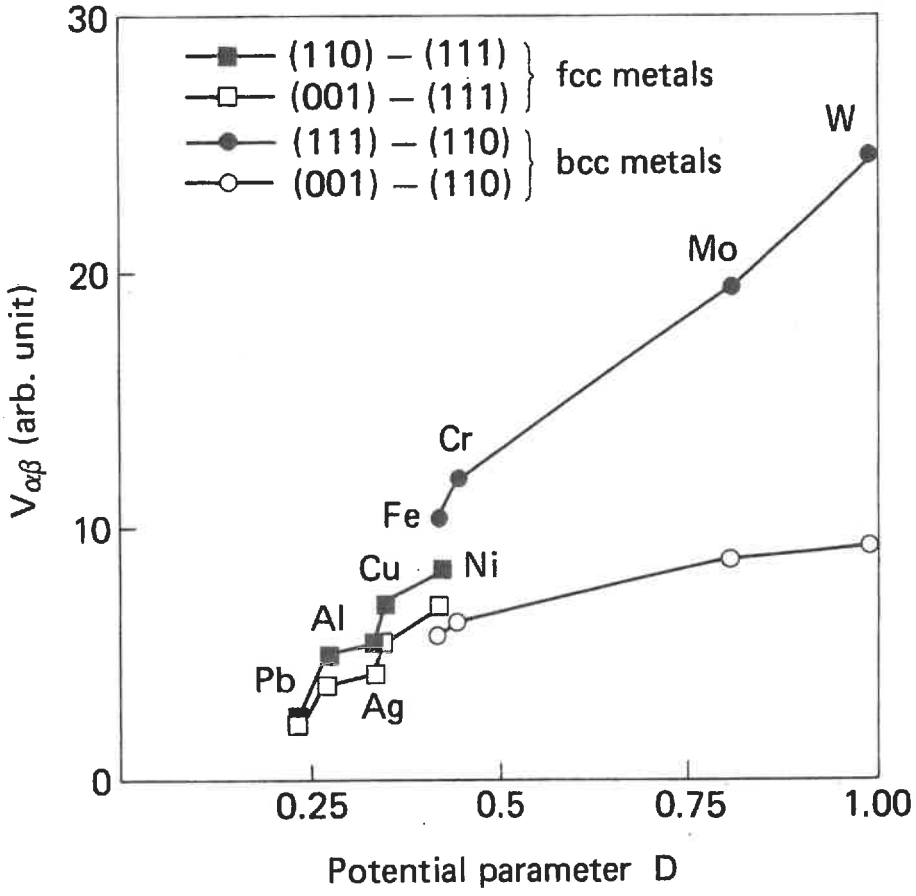

Figure 4.15: Calculated $V_{\alpha,\beta}$ as a function of Morse potential parameter D.

...) of the upper body by relaxation in the (111)-(110) contact. This is due to the fact that the atoms of the upper layers (2nd, 3rd, ...) move toward the local lowest minima more easily in the (111)-(110) contact, since the (111) plane has less density. These situations also hold true for the fcc metals in the same way.

4.6 Discussion and Conclusion: atomistic locking

Frictional properties were characterized by both the $\vec{Q}$-dependence of $P_1(\vec{r};\vec{g}_1,\vec{g}_2)$ and changes in the topological property of $P_1(\vec{r};\vec{g}_1,\vec{g}_2)$ that occurred due to the strength of interatomic potentials. The topological property of $P_1(\vec{r};\vec{g}_1,\vec{g}_2)$ is revealed in a pattern made by tiling $P_1(\vec{r};\vec{g}_1,\vec{g}_2)$ in a two-dimensional space. Frictional force vanishes when $P_1(\vec{r};\vec{g}_1,\vec{g}_2)$ is invariant with $\vec{Q}$ and its pattern is connected, but frictional force appears when $P_1(\vec{r};\vec{g}_1,\vec{g}_2)$ is variant with $\vec{Q}$ or the pattern is disconnected.

There are two atomistic origins for solid sliding friction; atomistic locking and dynamic locking. In atomistic locking, all the constituent atoms move continuously. Atomistic locking can occur for an arbitrary strength of potential $V^l(r)$. In the classical mechanical locking model, the (non flat) potential surface that the upper body feels from the lower body spans on a large scale. In atomistic locking, the (non flat) potential surface spans on a atomistic scale. On the other hand, in dynamic locking, the atoms discontinuously change their positions due to dynamic movements of the atoms. In contrast to atomistic locking, in dynamic locking the atoms non-adiabatically jump beyond potential barriers between neighboring sites. This origin cannot be described within the framework of the adiabatic potential. Dynamic locking follows disconnectedness of the connected pattern of a tiled $P_1(\vec{r};\vec{g}_1,\vec{g}_2)$ as $V^l(r)$ increases.

The criterion for the occurrence of friction transition was obtained. From studying the frictional properties of various systems, it can be concluded that friction transition may not appear for realistic systems, which suggests that atomistic locking is responsible for the solid sliding friction in these systems. friction force due to atomistic locking was calculated for an α-iron. Average friction force, as normalized by the contact area for a (001)-(001) contact of an α-iron, is estimated to be 7.6 GPa. This frictional force will be comparable to the frictional force that is measured in future. Another important conclusion is that a frictionless system is apparently possible if clean solid surfaces are prepared. The performance of the experiments to confirm this possibility will be a highly desirable goal for the future.

A mechanism for solid friction similar to mine was proposed by Tomlinson [66]. He explained that the origin of solid sliding friction stems from dissipation of the elastic energy introduced by the relative sliding motion of two contacting solid bodies. This elastic energy is stored by an atom and is transformed into vibrational (or kinetic) energy, then is subsequently dissipated through the surrounding atoms. The sum of the independently lost elastic energy stored by each atom is ascribed to the energy required to slide two contacting surfaces. His idea is different from mine, however, since he does not consider possible cooperative movements by the constituent atoms.

Further investigations on the dynamical properties of friction and frictional systems having non-crystalline surfaces, which has been experimentally observed for metals and ceramics, will be presented in future.

Chapter 5

Dynamics of Friction: Superlubric state

5.1 Introduction

The (dynamic) friction force is the drag against sliding, appearing when two solid surfaces move relatively [11]. Then, the energy is dissipated during sliding. The friction is a problem of how the energy can be dissipated. The data of friction forces usually measured contains many unknown factors: surface roughness, fractures, plastic deformations, poisoning by contaminants such as O_2, H_2 and oil, etc. It is difficult, therefore, to study the origin of friction force from the experimental data available at present. More recent experimental studies [13] try to exclude many of the unknown factors by preparing well-defined surfaces.

This chapter theoretically considers the dynamic properties in friction by assuming two clean solid surfaces, which is generated by intrinsic factors, such as molecular interactions between constituent atoms, not by extrinsic factors such as surface asperities or surface contaminants. Friction is formulated as a problem of whether or not given (sliding) kinetic energy for the translational motion dissipates into the kinetic energies for the internal motions during sliding. We shall study the dynamics in friction by using the Frenkel-Kontorova model with kinetic energy terms.

5.2 Preliminaries: nonadiabatic motion of atoms

Tomlinson [66] has first pointed out an importance of nonadiabatic motion of atoms. Let us describe an essence of his idea. Suppose the friction system consisting of two atoms numbered by 1 and 2, as seen in fig. 5.1. Two atoms are assumed to interact with each other. The atom 1 forms a part of the upper solid surface, which interacts with other atoms of the upper solid surface simply by the spring, while the atoms 2 form a part of the lower solid surface, which is assumed to be fixed. We shall concentrate the behavior of the atom 1 when the upper surface slowly slides against the lower surface. When the atom 1 is in the left side of the atom 2, the spring does not bend. As the atom 1 moves towards the right direction, the spring begins to bend. When the sliding displacement is small, this is a process of storing the elastic energy in the spring. When the atom 1 goes beyond the certain distance, he assumes that the atom 1 non-adiabatically (abruptly) changes its

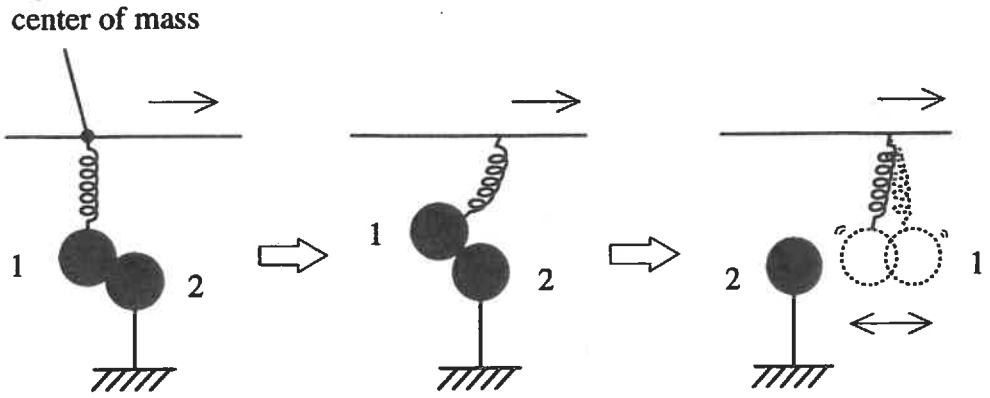

Figure 5.1: Nonadiabatic motion of atom.

position. The non-adiabaticity leads to transforming the elastic energy of the spring into the vibrational or kinetic energy of the atom 1. The vibrational energy of the atom 1 may be considered to dissipate into the vibrational energies of other atoms, i.e., into the thermal energy. Mori et al. proposes the same idea [67, 42]. If the atom 1 is assumed only to change its position slowly, the atom 1 may not take an excess kinetic energy, which can be concluded from the adiabatic theorem.

On the other hand, similar nonadiabatic motion occurs also for the systems of many atoms such as the low dimensional systems such as the one-dimensional Frenkel-Kontorova model, the discrete model of the charge density wave, and so on. The occurrence of such nonadiabatic motion is one of the phenomena of the Aubry transition [58]. The atoms can move by changing their equilibrium positions discontinuously during sliding [39, 23, 42].

We, however, concluded [23] that the nonadiabatic motion of atoms does not occur in the realistic (three dimensional) friction systems by deriving the condition for the occurrence of such nonadiabaticity and examining it in the various friction systems. This was made by assuming a quasistatic sliding where atoms take the most stable configuration. Here, it is studied the dynamic property in friction in which the atoms do not take the stable configuration.

5.3 Friction model

5.3.1 Equations of motion

Let us consider the following friction system given by

$$H(\{p_i\},\{q_i\}) = \sum_i^N \frac{p_i^2}{2} + \sum_i^N \{\frac{1}{2}\sum_{j(\neq i)}^N v_1(q_i - q_j) + v_2(q_i)\}, \tag{5.1}$$

where N ($\gg 1$) denotes the number of the atoms of the upper solid surface. The first, the second, and the third term of the right hand side stand for the kinetic energy of the ith atom, the mutual interactions between the atoms of the upper solid surface, and the adhesion energy given by $v_2(q) \equiv \sum_j v_a(q - q_j)$ ($v_a(q - q_j)$: the interaction energy from the jth atom of the lower surface), respectively. The lower solid surface is assumed to be rigid, and so the relevant degrees of freedom is dropped from the considerations in eq.(5.1). In the friction process, it is convenient to distinguish the translational degree of freedom, i.e., the center of mass, of the upper surface from the other degrees of freedom concerning with the internal motions. The notations ($P = \sum_i^N p_i/N$,$Q = \sum_i^N q_i/N$) and ($\bar{p}_i = p_i - P, \bar{q}_i = q_i - Q$) ($i = 1, 2, .., 3(N-1)$), where P and Q are, respectively, the momentum and the coordinate of the center of mass, specifying the translational motion, and $\bar{p}_i$ and $\bar{q}_i$ are, respectively, the momentum and the position coordinate of the ith atom, specifying the internal motions, are introduced. In other words, P corresponds to the sliding velocity of the upper surface. The quantities which are interested in are P and Q, which specify sliding of the upper surface. By using these notations, the friction system can be rewritten by

$$H(\{\bar{p}_i\}, \{\bar{q}_i\}; P, Q) = N\frac{P^2}{2} + \sum_i v_2(\bar{q}_i + Q) + H_0(\{\bar{p}_i\}, \{\bar{q}_i\}), \tag{5.2}$$

$$H_0(\{\bar{p}_i\}, \{\bar{q}_i\}) = \sum_i^{N-1} \frac{\bar{p}_i^2}{2} + \frac{1}{2}\sum_{i\neq j}^{N-1} v_1(\bar{q}_i - \bar{q}_j). \tag{5.3}$$

$H_0(\{\bar{p}_i\}, \{\bar{q}_i\})$ involves only degrees of freedom for the internal motions, and the translational motion (P, Q) is connected with the internal motions $(\bar{p}_i, \bar{q}_i)$ by the second term, i.e., the adhesion term in the right hand side of eq.(5.2). The motion of equation for the center of mass of the upper surface is given from eq.(5.3):

$$\frac{dP}{dt} = \frac{1}{N}F_d(t)$$

and

$$\frac{dQ}{dt} = P, \tag{5.4}$$

where $F_d(t)$ is a friction force, defined by

$$F_d(t) = -\sum_i \frac{\partial v_2(\bar{q}_i(t) + Q(t))}{\partial Q}. \tag{5.5}$$

The equations for the internal motions are written from eq.(5.2),

$$\frac{d\bar{p}_i}{dt} + \sum_j \frac{\partial v_1(\bar{q}_i(t) - \bar{q}_j(t))}{\partial \bar{q}_i} = f_i(\bar{q}_i(t) + Q(t))$$

and

$$\frac{d\bar{q}_i}{dt} = \bar{p}_i, \tag{5.6}$$

where $f_i(\bar{q}_i(t) + Q(t))$ is a driven force acting on the internal motions, defined by $f_i(\bar{q}_i + Q(t)) = -\partial v_2(\bar{q}_i + Q(t))/\partial \bar{q}_i$.

5.3.2 Friction diagram

Let us study the friction system in eq.(5.1), given by

$$H(\{p_i\},\{q_i\}) = \sum_i^N \frac{p_i^2}{2} + \sum_i^N \{\frac{1}{2}(q_{i+1} - q_i - \ell)^2 + \frac{k_1}{2\pi}\sin(2\pi q_i)\}, \tag{5.7}$$

where k_1 stands for the strength of the adhesion interaction. This is one dimensional Frenkel-Kontorova model [68, 69] with kinetic energy terms. The ℓ is the mean distance between two adjacent atoms. (Note that the periodicity length of the sinusoidal potential in eq.(5.7) is taken as a unit.) The Frenkel-Kontorova model has been studied by many workers. It is known that this model shows nonadiabatic motion of atoms, as mentioned in section 2, near at $k_1 \simeq 0.14$, which is often called the Aubry transition point [58]. We shall study the dynamics in friction by adding the kinetic energy terms to the model.

To examine the friction property, we shall study the dynamics after the upper solid surface at the ground state is pushed with initial sliding velocity $P(0)$ ($\bar{p}_i(0) = 0$ for any i), that is, the Hamiltonian dynamics conserving the energy. The dynamics is studied by by examining quantities such as $P(t)$, $Q(t)$, $\bar{q}_i(t)$, $\bar{p}_i(t)$ and the sliding distance $l_s(t)$ defined as the distance over which the upper solid surface slides during time t. These quantities are obtained by solving eqs.(5.4)-(5.7). The ℓ is assumed to be equal to the golden mean number $(\sqrt{5}+1)/2$. Two regimes appear in the diagram shown in fig.2; In the superlubricity regime, the superlubric state appears, i.e., two contacting solid surfaces slide without any resistance. The recurrence phenomenon occurs persistently; this regime repeats increasing and decreasing the translational kinetic energy with time. The friction force $F_d(t)$ averaged over the recurrence time exactly vanishes. The sliding distance $l_s(t)$ increases linearly with time: $l_s(t) = c[P(0)]t$. The $c[P(0)]$ is a averaged velocity satisfying $c[P(0)] \leq P(0)$, and depends on $P(0)$. On the other hand, in the friction regime, the energy dissipation occurs; The translational kinetic energy is transferred into the kinetic energy of the internal motions. The upper surface slides but finally ceases to slide: $l_s(t) < \infty$ for sufficiently large t. The friction occurs in this regime. As $P(0)$ becomes smaller, the sliding distance decreases for the region $k_1 \geq 0.14$. The point at $k_1 \simeq 0.14$ and $P(0) = 0$ is the Aubry transition point: in the regime $k_1 > 0.14$, the atoms change their equilibrium positions discontinuously. This was described in §2. In the regime $k_1 < 0.14$ and $P(0) = 0$, the atoms can slide by changing their equilibrium positions continuously, and the system can slide without any resistance. Nevertheless, the friction regime spreads on the region $0.06 < k_1 < 0.14$ with finite $P(0)$. This is different from the result for the pure Frenkel-Kontorova model without any kinetic energy terms, and is due to a dynamic effect of the system [1] . In particular, the distance, $l_s(\infty)$, over which the upper solid surface runs till it ceases to slide is $l_s(\infty) \simeq 1$ as the parameters k_1 (>0.14) and $P(0)$ approach near the horizontal axis, while $l_s(t)$ tends to stretch with time t as one approaches the border line separating the friction regime from the superlubricity regime. In the friction regime, the temporal behavior of the friction force $F_d(t)$ depends on $P(0)$ and k_1 in a complex manner. As the parameter k_1 means the strength of the adhesion between the upper and the lower

[1] The simulations presented here show that the potential energy $v(Q) = \sum_i v_2(\bar{q}_i + Q)$ in eq.(5.2) for the center of mass takes a multivalued function of Q, implying that there are the different timescales for the internal relative motions and for the translational motion.

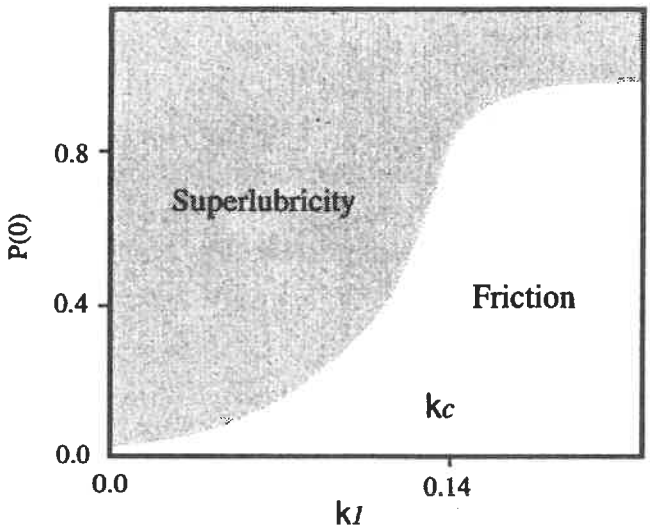

Figure 5.2: Friction diagram for the one dimensional Frenkel-Kontorova model with kinetic energy terms.

solid surfaces, $k_1 \leq k_{wa}$, say $k_{wa} \simeq 0.1$, corresponds to the weak adhesion. (Note that the strength of interaction between atoms of the upper solid surface is set equal to unity.) The diagram in Fig. 5.2 shows that the superlubric state appears only for two cases of the weak adhesion and of the high sliding velocity. The property that the superlubricity appears only for the weak adhesion is peculiar for the one-dimensional system. This point will be discussed later, concerning with the dimensionality of the system.

5.4 Frictional property

5.4.1 Superlubricity

In the superlubricity regime, two contacting solid surfaces can slide with no resistance. A generic consideration of eqs.(5.4) and (5.5) concludes that the superlubric state appears when the system satisfies either of two following conditions: (I) $\sum v_2(\bar{q}_i(t)+Q(t))$ in eq.(5.5), hereafter denoted by $v(Q(t))$, has no Q-dependence, and (II) the persistent recurrence phenomenon occurs. (I) is concluded from eqs.(5.4) and (5.5), and (II) was described in the previous subsection 5.3.2. The second condition may be a special case of (I) if $v(Q(t))$ is regarded as the quantity averaged over the recurrence time.

Then, there arises a problem of how to construct the friction systems showing the superlubricity. One among them, for examples, is to prepare the friction system consisting of two clean flat solid surfaces, as studied in previous sections. The condition (I) has been discussed as the condition for the phason mode to exist, and can be replaced by another two conditions: (I-1) the quasistatic sliding: the sliding velocity is so slow that the atoms follow their equilibrium positions adiabatically and (I-2) two solid surfaces contact incommensurately [23]. The nonadiabatic motion of atoms seen in section 5.2 do not occur if

these are both satisfied. On the other hand, the condition (II) is first pointed out here, which is a result of the dynamic effect of the system.

5.4.2 High dimensionality

This section aims to emphasize an importance of high dimensionality in the friction system, which makes the superlubricity appear much easily. By the term 'dimensionality', we mean the number of the spatial directions towards which the atoms can move or relax during sliding. The importance of high dimensionality is demonstrated by using two dimensional Frenkel-Kontorova model analogous to that in eq.(5.7), given by

$$\begin{aligned} & H(\{p_{i,j}\}\{q_{i,j}\}) \\ &= \sum_{i}^{N} \frac{1}{2}({p_{i,i}^{x}}^2 + {p_{i,i}^{y}}^2) \\ &+ \sum_{i,j}^{N} \{\frac{1}{2}[(q_{i+1,j}^{x} - q_{i,j}^{x} - \ell)^2 + (q_{j,i+1}^{y} - q_{j,i}^{y} - \ell)^2] \\ &+ \frac{k_1}{\pi}\cos\{\pi[q_{i,j}^{x}(\cos\theta + \sin\theta) + q_{i,j}^{y}(\cos\theta - \sin\theta)]\} \\ &\times \cos\{\pi[q_{i,j}^{x}(\cos\theta - \sin\theta) + q_{i,j}^{y}(\text{-}\cos\theta + \sin\theta)]\}, \end{aligned} \tag{5.8}$$

where atoms arrange on the square lattice points specified by two index numbers i and j. The position and momentum of the (i,j)th atom are, respectively, denoted by $q_{i,j}=(q_{i,j}^{x}, q_{i,j}^{y})$ and $p_{i,j}=(p_{i,j}^{x}, p_{i,j}^{y})$. The θ is a lattice misfit angle between the upper and lower solid surfaces with square lattice symmetry. The calculations are made similar to those in section (3.B). The upper solid surface is pushed with initial sliding velocity $P(0)$=0.02 along x-direction, or equivalently, along the θ-direction against the lower surface. The dynamic property for the case $\theta = 0°$ or $90°$ becomes identical to that of the one-dimensional Frenkel-Kontorova model, as easily seen from eq.(4.1). The case $\theta = 45°$ gives the largest critical value k_c ($\simeq 0.25$), which is about 4 times of k_c ($\simeq 0.06$) of the one-dimensional case, which is seen from the diagram in Fig. 4.7. For the parameter $k_1 \leq k_c$, the superlubric state appears.

Why does the critical value k_c arise for the two dimensional Frenkel-Kontorova model? This is explained as follows; Suppose two dimensional friction system where the lower solid surface is assumed to have a square lattice symmetry, as shown in fig. 5.3. The region where each atom of the upper solid surface can move without occurring the nonadiabatic motion described in section 5.2 is shown by shade part, while the region where the nonadiabatic motion occurs by empty part. Two dimensions allow the atoms to move by changing its position flexibly in the shaded region. Therefore, the atom can slide avoiding the region where the nonadiabatic motion occurs, as shown by arrow. The appearance of nonadiabatic region does not mean that the superlubric state breaks down. This should be compared with the case of one-dimensional systems. When the dimensionality arises further, the atoms can move more flexibly. For the three dimensional friction systems, it as shown that the critical value k_c becomes much larger than that calculated for the realistic systems: the superlubric state appear for any combinations of metals with clean and flat surfaces. (The metals were simulated by using the Morse type potentials determined empirically.) The possibility for the superlubric state to appear has been discussed by other workers [39, 42].

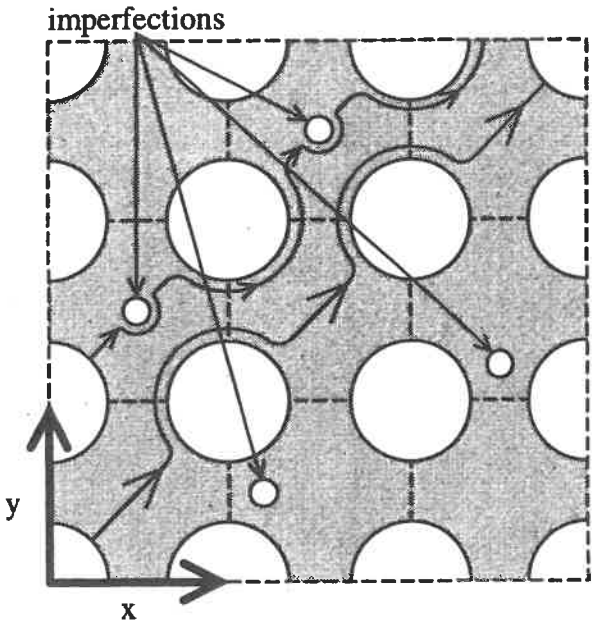

Figure 5.3: Sketch of the region where the atom can move by changing its position flexibly, which is shown by shaded part.

They was based on the result for the case of the one-dimensional systems with $P(0) = 0$, and concluded that it appears only for the case of the weak adhesion. The above analysis shows that the superlubricity is a generic phenomenon, and appears for a wide class of the (strong or weak) adhesion including the metallic bonding and the Van der Waals interaction [23]. High dimensionality is a key to understand the physics of superlubricity.

5.5 Discussion

It has been studied the dynamic property in friction from an atomistic point of view. Let us compare the results with those obtained [23] by assuming the (quasistaically sliding) case where the upper surfaces slides with very low velocity. From the study of Frenkel-Kontorova model with kinetic energy terms, it was found that superlubricity appears even for the case with finite sliding velocity as well as for the quasistaically sliding case. Superlubricity occurs due to the persistent recurrence phenomenon where the translational kinetic energy repeatedly increases and decreases with time. It has been emphasized that for high dimensional systems, superlubricity is a generic phenomenon, appearing for a wide class of (strong or weak) adhesion such as metallic bond and van der Waals interaction.

The superlubricity phenomenon is interesting from both theoretical and applicable points of view. To confirm an existence of superlubric state, The experiment[20] was done by using two contacting muscovite mica. The experiments confirmed that the friction forces become smaller as the experimental conditions approach being those for the appearance of the superlubric state. Although it was not mentioned in subsection 5.4.2, the high dimensionality yields another remarkable property in the friction. The friction becomes anisotropic with respect to the lattice misfit angle θ between the upper and the lower solid surfaces: for examples, for the case of two dimensional Frenkel-Kontorova model with

$k_1 = 0.2$ and the sliding velocity $P(0) = 0.02$, the friction appears for the misfit angle $\theta = 0°$ and vanishes for $\theta = 45°$. In fact, we have also observed the anisotropy of friction in the above experiment [20]. For the applicable viewpoint, the anisotropy implies a feasibility for controlling friction and designing friction systems by taking the lattice misfit angle as a controlling parameter.

Chapter 6

Concluding Remarks

Frictional properties were studied from an atomistic point of view. In the first part of this thesis, it was observed that friction forces of clean surfaces greatly depend on the lattice misfit between contacting surfaces. In the first experiment, in Chapter 2, the friction forces of single crystal muscovite mica were measured as a function of the lattice misfit between the two contacting cleavage surfaces, and it was found that the friction forces are anisotropic with respect to the lattice misfit angle, i.e., they increase (decrease) when the surfaces contact without (with) lattice misfit along sliding direction. It was concluded that the observed frictional anisotropy stems from the change in the lattice misfit between contacting lattices as predicted by the theory presented in Chapter 4. In the second experiment, in Chapter 3, it was also observed the frictional anisotropy in atomically clean surfaces by using atomically clean and well-defined surfaces [21, 22]. The friction forces of the atomically clean surfaces of Si(001) and W(011) are measured as a function of the lattice misfit along the sliding direction between the clean surfaces under ultra-high vacuum by scanning tunneling microscopy. Friction was not observed when the surfaces contact with lattice misfit along sliding direction in measurements capable of resolving a friction force of 3×10^{-9} N, whereas friction with a magnitude of 8×10^{-8} N, which is comparable to theoretical values, was observed when the surfaces contact without lattice misfit along the sliding direction. It was concluded that the observed dependence of friction force on the lattice misfit of the contacting surfaces agrees with the theoretical predictions made in Chapter 4.

The latter half of thesis theoretically studied the atomistic origin of the friction force intrinsically generated by the molecular interactions between the constituent atoms of solids [23, 24]. In Chapter 4, it was shown that there are two origins: *atomistic locking* and *dynamic locking* [23]. Atomistic locking occurs when the configuration of atoms on a contact surface continuously changes with the sliding distance and when the interatomic potentials have an arbitrary strength. Dynamic locking occurs when the configuration changes discontinuously due to the dynamic process and if the interatomic potential is stronger than a specific given value. It was concluded that dynamic locking is unlikely to occur in realistic systems from studying various systems. Based on that conclusion, the theory predicted that "superlubricity", in which friction force completely vanishes in infinite systems at the limit of zero sliding speed, does appear in realistic systems. In chapter 5, it was studied that the dynamic property in friction from an atomistic point of view. From the study of the Frenkel-Kontorova model with kinetic energy terms, it was

found that superlubricity appears even for the case with finite sliding velocity as well as for the quasistatic sliding discussed in Chapter 4. Superlubricity occurs due to the persistent recurrence phenomenon where the translational kinetic energy repeatedly increases and decreases with time. It was emphasized that for high-dimensional systems, superlubricity is a generic phenomenon, appearing for a wide class of (strong or weak) adhesion such as metallic bond and van der Waals interaction.

Friction research based on atomistic theory has created a new stage for friction research. On that new stage, the theoretical origins of friction and the state of superlubricity are clearly displayed, and the appropriateness of conclusions regarding them is being determined by experiments that have identified the factors involved in friction phenomena. On the theoretical front, Matsukawa and Fukuyama are investigating the atomistic-theoretical laws of friction [44]. On the experimental front, a group at Ecole Centrale de Lyon has begun experiments to verify superlubricity using MoS_2 [49]. The concept of superlubricity also provides a new perspective on methods for controlling friction and for understanding friction in biological systems.

One application of superlubricity is to control friction, which can be done by making use of the anisotropy of friction. Let's look again at the anisotropy of friction in Fig. 2.4 from the viewpoint of application. Experiments with mica have demonstrated that the friction force varies with the degree of lattice misfit between the two surfaces, which supports theoretical predictions of anisotropy in friction. Therefore, the force of friction can be controlled by determining the lattice misfit, in which case the degree of lattice misfit becomes the control variable. For mica, the controllable range of the coefficient of friction is from 0.16 to 0.63.

The concept of superlubricity provides a new perspective on friction and movement in biological systems, such as flagellar [70] and muscle tissue [71]. The salmonella bacterium, which is about 1 μm in size, moves by means of flagellar that rotate at high speed (several tens of thousands of revolutions per minute). That high-speed rotation, however, does not destroy the bearing at the base of the flagellum. The friction in this sort of micro-scale bearing is thought to be small because of the energy recursion phenomenon, which appears in micro-scale systems such as molecular-level mechanisms in biological systems or micro-machines. In the contraction of muscle tissue, the two proteins actin and myosin slide one-dimensionally in a particular direction with high work efficiency (80% for turtle muscle), powered by the hydrolysis of ATP. Anisotropy in which the friction between actin and myosin is low in one direction and high in the opposite direction is considered to play a role in the mechanism for this one-dimensional sliding motion in a particular direction. If this kind of anisotropy exists, then the sliding motion will occur more easily in the direction of lower friction, even if the driving force for the motion is non-directional, thus resulting in the one-dimensional sliding motion.

It might be thought that atomistic friction is idealized, and that it is widely different from the friction dealt with in tribology. I believe, however, that research on friction requires an approach that goes beyond such common-sense thinking. Indeed, research on extraordinary phenomena such as superconductivity and nuclear fusion have greatly broadened the realm of science and technology. That is to say, the paradoxes of common-sense thinking are the stimuli for scientific advancement. We must go on to create a new stage for friction research.

Appendix A

Appendix

The frictional properties are considered by taking mutual interaction U into account. Adiabatic potential is expressed with an approximation that neglects the higher order terms rather than the second order term of Δr_i^α:

$$W(\vec{Q}) = \sum_i V^l(r_{i0}^1) + \sum_i V^u(r_{i,0}^1) + \sum_{i,j} V_{aa}(|\vec{r}_{i,0}^1 - \vec{r}_{j,0}^1|)$$
$$+ \sum_{i,\alpha} \frac{\partial V^l(r_{i,0})}{r_{i,0}^\alpha} \times \Delta_i^\alpha + \frac{1}{2} \sum_{i,\alpha,\beta} [\epsilon_{i,j}\{V_{i,j}^{l\alpha,\beta} + V_{i,j}^{u\alpha,\beta}\} + U_{i,j}^{\alpha,\beta}] \times \Delta r_i^\alpha \Delta r_i^\beta. \quad \text{(A.1)}$$

By using orthogonal transformation

$$\Delta r_i^\alpha = \sum_{\vec{k}} c_{i;\vec{k},\lambda} q_{\vec{k},\lambda}, \quad \text{(A.2)}$$

where

$$\sum_i c_{i;\vec{k},\lambda}^* \times c_{i;\vec{k}',\lambda'} = \delta_{\vec{k};\vec{k}'} \delta_{\lambda,\lambda'}, \quad \text{(A.3)}$$

and

$$\sum_{\vec{k},\lambda} c_{i;\vec{k},\lambda}^* \times c_{j;\vec{k},\lambda} = \delta_{i,j}, \quad \text{(A.4)}$$

which diagonalizes the last term in the right hand side, giving

$$W(\vec{Q};\{q_{\vec{k},\lambda}\}) = \sum_i V^l(r_{i0}^1) + \sum_i V^u(r_{i,0}^1) + \sum_{i,j} V_{aa}(|\vec{r}_{i,0}^1 - \vec{r}_{j,0}^1|)$$
$$+ \sum_{\vec{k},\lambda} \gamma_{\vec{k},\lambda} q_{\vec{k},\lambda} + \frac{1}{2} \sum_{\vec{k},\lambda} \omega_{\vec{k},\lambda} q_{\vec{k},\lambda}^* q_{\vec{k},\lambda}, \quad \text{(A.5)}$$

where $\gamma_{\vec{k},\lambda}$ is defined by

$$\gamma_{\vec{k},\lambda} = \sum_{i,\alpha} \frac{\partial V^l(r)}{\partial r_{i,0}^{1,\alpha}} \times c_{i;\vec{k},\lambda}. \quad \text{(A.6)}$$

All eigenvalues $\omega_{\vec{k},\lambda}$ must be positive. When $V^l(r)$=0, displacement $q_{\vec{k},\lambda}$=0 from eq. $(A.6)$. So, from eq. $(A.2)$, $\Delta r_i^\alpha = 0$ for all i and α. For a non-vanishing $V^l(r)$, the displacement is

$$q_{\vec{k},\lambda} = -\frac{\gamma^*_{\vec{k},\lambda}}{\omega_{\vec{k},\lambda}}, \tag{A.7}$$

or

$$\begin{aligned}\Delta r_i^\alpha &= -\sum_{\vec{k},\lambda} \frac{c_{i;\vec{k},\lambda}\gamma^*_{\vec{k},\lambda}}{\omega_{\vec{k},\lambda}} \\ &= -\sum_{j,\vec{k},\lambda} \frac{c_{i;\vec{k},\lambda}\partial V(r)/\partial r^\alpha_{j,0} c^*_{j;\vec{k},\lambda}}{\omega_{\vec{k},\lambda}}.\end{aligned} \tag{A.8}$$

Below, the result in eq. (4.12) is derived for a weak mutual interaction U. When $V^u(r) >> U$, the dispersion of $\omega_{\vec{k},\lambda}$ is negligible. If $\omega_{\vec{k},\lambda}$=ω_0 for all $\vec{k}$ in $(A.8)$, we have

$$\begin{aligned}\Delta r_i^\alpha &= -\sum_{j,\vec{k},\lambda} \frac{c_{i;\vec{k},\lambda}\partial V(r)/\partial r^\alpha_{j,0} c^*_{j;\vec{k},\lambda}}{\omega_{\vec{k},\lambda}}, \\ &= -\frac{1}{\omega_0}\sum_{j,\vec{k},\lambda} c_{i;\vec{k},\lambda}\frac{\partial V(r)}{\partial r^\alpha_{j,0}} c^*_{j;\vec{k},\lambda},\end{aligned} \tag{A.9}$$

by using the condition of normalization for $c_{i;\vec{k},\lambda}$ in $(A.2)-(A.3)$,

$$\begin{aligned}&= -\frac{1}{\omega_0}\sum_j \delta_{i,j}\frac{\partial V(r)}{\partial r^\alpha_{j,0}}, \\ &= -\frac{1}{\omega_0}\frac{\partial V(r)}{\partial r^\alpha_{i,0}},\end{aligned} \tag{A.10}$$

This completes the proof of eq. (4.12).

Next the criterion for the friction transition is derived. The ridge lines of $V^l(r)$ correspond to the lines satisfying $\Delta r_i^\alpha = 0$, or equivalently

$$0 = -\sum_{j,\vec{k},\lambda} \frac{c_{i;\vec{k},\lambda}\partial V(r_j)/\partial r^\alpha_{j,0} c^*_{j;\vec{k},\lambda}}{\omega_{\vec{k},\lambda}}. \tag{A.11}$$

The criterion for the occurrence of friction transition is to see if the pattern obtained by tiling $P_1(\vec{r};\vec{g}_1,\vec{g}_2)$ is connected or disconnected along the ridge lines.

Bibliography

[1] For a review involving history in the field of friction see, e.g., 曾田範宗, 摩擦のはなし (Iwanami- Shoten, Tokyo, 1971).

[2] 曾田範宗, 機械学会誌 **81**, 719, 1016 (1978).

[3] For a review see, e.g., D. Dowson, *J. Lub. Technol., Trans. ASME* **99**, 383 (1977).

[4] D. Dowson, *J. Lub. Technol., Trans. ASME* **100**, 3 (1978).

[5] D. Dowson, *J. Lub. Technol., Trans. ASME* **100**, 148 (1978).

[6] R. Holm, in *Electric Contacts* (Spring Verlag, Berlin, 1967).

[7] D. Tabor, *J. Lub. Technol., Trans. ASME* **103**, 169 (1981).

[8] C. A. Coulomb, *Mémories de Mathematique et de Physics de l'Acaddemie Royale*, 161 (1785).

[9] J. T. Desaguliers, *A Course of Experimental Philosophy Vols. 2.*

[10] J. T. Desaguliers, *Phil. Trans. Roy. Soc. (London)* **33**, 345 (1725).

[11] F. P. Bowden and D. Tabor, in *Friction and Lubrication of Solids, Vol II* (Clarendon Press, Oxford, 1964).

[12] D. Tabor, *Proc. Roy. Soc. Lond.* A**251**, 1266 (1959).

[13] C. M. Mate, G. M. McClelland, R. Erlandsson, and S. Chiang, *Phys. Rev. Lett.* **59**, 1942 (1987).

[14] R. Kaneko, K. Nonaka and K. Yasuda, *J. Vac. Sci. Technol.* **A6**, 291 (1988).

[15] G. Binnig, H. Rohrer, Ch. Gerber, and E. Weibel, *Appl. Phys. Lett.* **40**, 178 (1982).

[16] G. Binnig, H. Rohrer, Ch. Gerber, and E. Weibel, *Phys. Rev. Lett.* **49**, 57 (1982).

[17] G. Binnig, C. F. Quate, and Ch. Gerber, *Phys. Rev. Lett.*, **56**, 930 (1986).

[18] E. Meyer, R. Overney, D. Brodbeck, L. Howald, R. Lüthi, J. Frommer, and H.-J. Güntherodt, *Phys. Rev. Lett.* **69**, 1777 (1992).

[19] M. Mehregany, S. F. Bart, L. S. Tavrow, J. H. Lang, S. D. Senturia, and M. F. Schlecht, *Sensors and Actuators* **A**21 - **A**23, 173 (1990).

[20] M. Hirano, K. Shinjo, R. Kaneko, and Y. Murata, *Phys. Rev. Lett.* **67**, 2642 (1991).

[21] M. Hirano, K. Shinjo, R. Kaneko, and Y. Murata, in *Proc. of American Vacuum Society 41st National Symposium, Colorado, October 1994,* p. 291.

[22] M. Hirano, K. Shinjo, R. Kaneko, and Y. Murata, *Phys. Rev. Lett.* **78**, 1448 (1997).

[23] M. Hirano and K. Shinjo, *Phys. Rev.* **B41**, 11837 (1990).

[24] K. Shinjo and M. Hirano, *Surf. Sci.* **283**, 473 (1993).

[25] Y. Enomoto and D. Tabor, *Proc. R. Soc. Lond.* A**373**, 405 (1981).

[26] D. H. Buckley, *ASLE Trans.* **11**, 89 (1968).

[27] R. Takagi and Y. Tsuya, *Wear* **4**, 216 (1961).

[28] Y. Tsuya, *Wear* **14**, 309 (1969).

[29] D. H. Buckley and K. Miyoshi, in *Structural Ceramics*, edited by J. B. Watchman, Jr. (Academic Press Inc., San Diego, CA), Vol. 29, p.300.

[30] R. Erlandsson, G. Hadziioannou, C. M. Mate, G. M. McClelland, and S. Chiang, *J. Chem. Phys.* **89**, 5190 (1988).

[31] P. M. McGuiggan and J. N. Israelachvili, *Chem. Phys. Lett.*, **149**, 469 (1988).

[32] P. M. McGuiggan and J. N. Israelachvili, *J. Mater. Res.* **5**, 2232 (1990).

[33] W. L. Bragg, in *Atomic structure of minerals*, **205** (Cornell University Press, Ithaca, 1937).

[34] G. Simmons and H. Wang, in *Single Crystal Elastic Constants and Calculated Aggregate Properties* (The MIT Press, Boston, 1971).

[35] E. W. Radoslovich, *Acta Cryst.*, **13**, 919 (1960).

[36] K. Kinoshita, H. Kojima, and H. Yokota, *Jpn. J. Appl. Phys.*, **1**, 234 (1962).

[37] R. Kaneko, S. Oguchi, T. Miyamoto, Y. Andho and S. Miyake, *American Soc. of Tribologists and Lub. Eng., Special Publication* SP-29.

[38] B. Drake, C. B. Prater, A. L. Weisenhorn, S. A. C. Gould, T. R. Albrecht, C. F. Quate, D. S. Cannel, H. G. Hansma, and P. K. Hansma, *Science*, **243**, 1586 (1989).

[39] J. B. Sokoloff, *Surf. Sci.* **144**, 267 (1984).

[40] J. B. Sokoloff, *Phys. Rev.* **B31**, 2270 (1985).

[41] J. B. Sokoloff, *Phys. Rev.* B**42**, 760(1990).

[42] G. M. McClelland, in *Adhesion and friction, Springer Series in Surface Science*, edited by M. Grunze and H. J. Kreuzer (Springer Verlag, Berlin, 1990) Vol. 17, p. 1.

[43] H. Matsukawa and H. Fukuyama, *Phys. Rev.* B **49**, 17286 (1994).

[44] 松川 宏, 福山秀敏, 固体物理 **28** 10, 686 (1993).

[45] 新上和正, 数理科学 **10**, 17 (1993).

[46] 平野元久, 新上和正, 金子礼三, *NTT R & D* **40**, 869 (1991).

[47] 新上和正, 平野元久, 物性研究 **55**, 577 (1991).

[48] 平野元久, 数理科学 **10**, 23 (1993).

[49] J. M. Martin, C. Donnet, Th. Le Mogne, and Th. Epicier, *Phys. Rev.* B **48**, 10583 (1993).

[50] U. Dürig, J. K. Gimzewski, and D. W. Pohl, *Phys. Rev. Lett.* **57**, 2403 (1986).

[51] S. L. Tang, J. Bokor, and R. H. Storz, *Appl. Phys. Lett.* **52**, 189 (1988).

[52] K. Kuroda, S. Hosoki, and T. Komoda, *Scanning Microscopy* **1**, 911 (1987).

[53] T. Kohno, N. Ozawa, K. Miyamoto, and T. Musya, *Appl. Optics* **27**, 103 (1988); ZP-01 (Olympus Optical Co., Ltd., Tokyo, Japan).

[54] R. Gomer, in *Field Emission and Field Ionization* (Harvard University Press, Cambridge, 1961).

[55] E. W. Müller, *Z. Physik* **120**, 270 (1943).

[56] T. Tabata, T. Aruga, and Y. Murata, *Surf. Sci.* **179**, L63 (1987).

[57] See, e.g., V. I. Arnold and A. Avez, in *Problémes ergodiques de la mécanique classique* (Ganthier-Villas, Paris, 1967).

[58] S. Aubry, *J. Phys. (Paris)* **44**, 147 (1983).

[59] R. A. Johnson, *Phys. Rev.* **134**, 1329 (1964).

[60] H. M. Pak and M. Doyama, *J. Fac. Eng. Univ. Tokyo* **B30**, 111 (1969).

[61] Y. Waseda and S. Tamaki, *J. Solid State Phys. (Japan)* **1**, 133 (1976).

[62] L. A. Girifalco and V. G. Wezer, *Phys. Rev.* **114**, 687 (1959).

[63] R. Yamamoto, H. Matsuoka, and M. Doyama, *Phys. Stat. Sol.* (a) **51**, 163 (1979).

[64] A. T. Price, H. A. Holl, and A. P. Greenough, *Acta. Metall.* **12**, 49 (1964).

[65] J. S. McFarlane and D. Tabor, *Proc. Roy. Soc. Lond.* **A202**, 1069 (1950).

[66] G. A. Tomlinson, *Phil. Mag.* **7**, 905 (1929).

[67] Y. Mori, K. Endo, K. Yamamoto, Hui Wang, and T. Ide, *J. Jpn. Soc. Precision Engi. (in Japanese)* **56**, 679 (1990).

[68] Y. I. Frenkel and T. Kontorova, *Zh. Eksp. Teor. Fiz.* **8**, 1340 (1938).

[69] F. C. Frank and J. H. van der Merwe, *Proc. Roy. Soc.* **198**, 216 (1949).

[70] 相沢慎一, 鷲津正夫, 応用物理, **62**, 386 (1993).

[71] 柳田敏雄, 科学, **58**, 477 (1988).